

Evolving Nonthermal Electrons in Simulations of Black Hole Accretion

Andrew A. Chael^{1*}, Ramesh Narayan¹, Aleksander Sądowski^{2,3}

¹*Harvard-Smithsonian Center for Astrophysics, 60 Garden Street, Cambridge, MA 02138, USA*

²*MIT Kavli Institute for Astrophysics and Space Research, 77 Massachusetts Ave, Cambridge, MA 02139, USA*

³*Akuna Capital, 585 Massachusetts Ave, Cambridge, MA 02139, USA*

13 June 2017

ABSTRACT

Current simulations of hot accretion flows around black holes assume either a single-temperature gas or, at best, a two-temperature gas with thermal ions and electrons. However, processes like magnetic reconnection and shocks can accelerate electrons into a nonthermal distribution, which will not quickly thermalise at the very low densities found in many systems. Such nonthermal electrons have been invoked to explain the infrared and X-ray spectra and strong variability of Sagittarius A* (Sgr A*), the black hole at the Galactic Center. We present a method for self-consistent evolution of a nonthermal electron population in the GRMHD code KORAL. The electron distribution is tracked across Lorentz factor space and is evolved in space and time, in parallel with thermal electrons, thermal ions, and radiation. In the present study, for simplicity, energy injection into the nonthermal distribution is taken as a fixed fraction of the local electron viscous heating rate. Numerical results are presented for a model with a low mass accretion rate similar to that of Sgr A*. We find that the presence of a nonthermal population of electrons has negligible effect on the overall dynamics of the system. Due to our simple uniform particle injection prescription, the radiative power in the nonthermal simulation is enhanced at large radii. The energy distribution of the nonthermal electrons shows a synchrotron cooling break, with the break Lorentz factor varying with location and time, reflecting the complex interplay between the local viscous heating rate, magnetic field strength, and fluid velocity.

Key words: accretion, accretion discs – black hole physics – relativistic processes – methods: numerical – radiation mechanisms: non-thermal – Galaxy: centre

1 INTRODUCTION

Nearly every galaxy is thought to host a supermassive black hole at its centre, which accretes gas and liberates a large fraction of its binding energy in the form of radiation and outflows. Black hole accretion discs in active galactic nuclei often have luminosities close to the Eddington limit and are among the most luminous steady sources in the universe. In contrast, the black hole source at the centre of the Milky Way, Sagittarius A* (Sgr A*), has a low luminosity $\sim 10^{-9}$ of Eddington (Falcke et al. 1998; Genzel et al. 2003; Baganoff et al. 2003), and a correspondingly low mass accretion rate $\lesssim 10^{-7}$ of Eddington (Agol 2000; Bower et al. 2003; Marrone et al. 2007). The low luminosity of Sgr A* is due both to its low accretion rate and the low radiative efficiency of the accreting gas (Ichimaru 1977; Rees et al. 1982; Narayan & Yi 1995a,b; Blandford & Begelman 1999; Narayan et al.

1998; Quataert et al. 1999). Such radiatively inefficient or advection-dominated accretion flows (ADAFs) are geometrically thick and optically thin, and the gas is extremely hot (see Yuan & Narayan 2014 for a review).

When the density of the accreting gas is low, as in systems accreting below about 10^{-3} of the Eddington rate, Coulomb collisions between electrons and ions become rare, and the electron-ion thermalisation time exceeds the accretion time. Electrons and ions can then have different temperatures, with the ratio set by the balance between the viscous heating rates of the two species, the rate of energy transfer from ions to electrons by Coulomb coupling, and the rate of radiative cooling of the electrons. At the lowest densities, when the electron-electron collision time-scale becomes sufficiently long, collisions will not completely relax the electron distribution function to a local Maxwellian (Mahadevan & Quataert 1997). Even if the bulk of the electron distribution function is thermal, processes like shocks and magnetic reconnection (Sironi & Spitkovsky 2011, 2014) can accelerate

* E-mail: achael@cfa.harvard.edu

a small fraction of the electrons into a relativistic nonthermal distribution, which will persist for a long time because of the lack of collisions.

While traditional ADAF models emitting via thermal synchrotron radiation can describe the bulk of the emission from Sgr A* in the ‘submm bump’ around 10^{12} Hz (Narayan & Yi 1995b; Narayan et al. 1998; Quataert & Narayan 1999), the quiescent infrared and unresolved X-ray emission in the spectrum are most easily explained with hybrid models that include a small population of high-energy electrons in a power-law tail (Özel et al. 2000; Yuan et al. 2003, 2004; Broderick & Loeb 2006). In addition, Sgr A* is highly variable from the millimeter band to X-rays (Genzel et al. 2003; Eckart et al. 2006; Dodds-Eden et al. 2011). Analysis of 3D general relativistic magnetohydrodynamic (GRMHD) simulations has shown that synchrotron emission from the turbulent plasma, lensed by the central black hole, can produce variability in the infrared and sub-mm (Chan et al. 2015). Furthermore, thermal synchrotron emission in the infrared can be inverse Compton upscattered by the thermal electrons to higher frequencies, producing correlated variability in the X-rays (Ressler et al. 2017).

Observations of strong correlated flares ($\gtrsim 10$ times the quiescent flux) in the X-ray and infrared suggest that, in addition to the usual thermal electrons, there is rapid and localized injection of a broad nonthermal, power-law electron distribution that radiates strongly via synchrotron emission (Yusef-Zadeh et al. 2006; Dodds-Eden et al. 2009; Neilsen et al. 2013). Recently, Ball et al. (2016) took 3D GRMHD simulations from Narayan et al. (2012) and Sądowski et al. (2013) and moved a small percentage of the radiating electrons to a high-energy power-law distribution in regions of high magnetization. They showed that such a localized injection of nonthermal electrons produces correlated, broad-band variability in the infrared and X-ray flux, with variability properties similar to those observed in Sgr A*.

Numerical simulations of Sgr A* and other low accretion rate systems have typically been done within the context of single-fluid ideal magnetohydrodynamics (e.g. Hawley 2000; Tchekhovskoy et al. 2010; McKinney et al. 2012; Narayan et al. 2012), though recently Chandra et al. (2015); Foucart et al. (2016); Chandra et al. (2017) have incorporated the non-ideal MHD effect of anisotropic heat conduction. In order to produce spectra and images from simulations while taking into account the weak coupling between electrons and ions, the temperature ratio of the electrons to the total gas is usually set manually in post-processing. This ratio can be fixed globally, (e.g. Mościbrodzka et al. 2009; Dexter et al. 2010), vary depending on the region of the flow (disc or jet) under consideration (e.g. Mościbrodzka et al. 2014; Chan et al. 2015), or computed as a function of fluid properties (e.g. Shcherbakov et al. 2012). Including radiation from nonthermal electrons is less common, but some recent investigations have added a population of electrons with a power-law distribution of Lorentz factor during post-processing to investigate the effect on the quiescent spectrum and sub-mm image size of Sgr A* (Mao et al. 2016) and its variability properties (Ball et al. 2016).

Recent work (Ressler et al. 2015; Sądowski et al. 2017; Ressler et al. 2017) has extended single-fluid GRMHD simulations by introducing methods for self-consistent evolution of separate ion and electron populations. Ressler et al.

(2015, 2017) evolve a single-temperature non-radiative accretion flow and then evolve viscously heated electrons during a separate post-processing step. Sądowski et al. (2017) evolve ions and electrons simultaneously as two fluid components in a radiative magnetohydrodynamic simulation (GRRMHD), self-consistently including the effects of Coulomb coupling and radiative cooling (though these are not dynamically important, at least in the case of Sgr A*). Although the ions and electrons are treated as separate fluids in these studies, each species is still assumed to be independently in thermal equilibrium.

In this paper, we take the next logical step. Namely, in addition to evolving thermal ions, thermal electrons and radiation in a GRRMHD simulation, as in Sądowski et al. (2017), we also evolve a population of nonthermal electrons. The exchange of energy and momentum among the various fluid populations and the radiation field is accounted for at each time step during the evolution. The nonthermal electrons are heated by a prescribed fraction of the total viscous heating rate and they further gain and lose energy by adiabatic compression and expansion, Coulomb coupling, inverse Compton scattering, and radiative cooling. The algorithm is implemented in the GRRMHD code KORAL (Sądowski et al. 2013, 2014, 2017).

In Section 2, we review the standard GRMHD equations and present the additional equations needed for evolving the nonthermal population of electrons in the presence of radiation and Coulomb coupling. In Section 3, we describe the numerical algorithm, and in Section 4 we discuss a number of simple test problems that we have used to validate the code. In Section 5, we present initial results of a simulation of a Sgr A*-like accretion flow, which includes nonthermal electrons. We conclude with a summary in Section 6.

2 PHYSICS

2.1 Fluid Populations

GRMHD simulations typically track a single magnetized perfect fluid as a function of position and time. The single fluid is described by the gas density ρ , internal energy density u , and four-velocity u^μ . The pressure p is related to the internal energy u via the adiabatic index Γ_{int} ,

$$p = (\Gamma_{\text{int}} - 1)u. \quad (1)$$

In the ideal MHD approximation, the fluid frame electric field vanishes due to the high plasma conductivity. As a result, the electromagnetic field can be specified entirely via a magnetic field four-vector b^μ (Gammie et al. 2003). The MHD stress-energy tensor $T^\mu{}_\nu$ then takes the form

$$T^\mu{}_\nu = (\rho + u + p + b^2) u^\mu u_\nu + \left(p + \frac{1}{2}b^2\right) \delta^\mu{}_\nu - b^\mu b_\nu. \quad (2)$$

In the present work, the fluid consists of three populations: thermal ions, thermal electrons, and an isotropic distribution of nonthermal electrons. We assume that all three populations move with the same velocity u^μ . This assumption automatically preserves local charge neutrality and simplifies the evolution equations for the nonthermal spectrum (Section 2.4). Under this approximation, equation (2) remains a valid description of the total stress-energy, although

the equation of state relating p and u changes as explained below.

The electrons contribute negligibly to the mass density, hence,

$$\rho = \mu_i m_p n_i, \quad (3)$$

where m_p is the proton mass, μ_i is the ion mean molecular weight, and n_i is the fluid frame number density of ions. Denoting the electron mean molecular weight by μ_e , charge neutrality enforces the constraint

$$\mu_e (n_{e\text{th}} + n_{e\text{nth}}) = \mu_i n_i = \rho / m_p, \quad (4)$$

where $n_{e\text{th}}$, and $n_{e\text{nth}}$ are the number densities of the thermal and nonthermal electrons, respectively. In the simulations presented in this paper we consider only pure ionized hydrogen: $\mu_i = \mu_e = 1$.

All three fluid populations can have substantial contributions to the net energy density and pressure,

$$\begin{aligned} u &= u_i + u_{e\text{th}} + u_{e\text{nth}}, \\ p &= p_i + p_{e\text{th}} + p_{e\text{nth}}. \end{aligned} \quad (5)$$

The energy densities and pressures of the thermal species are determined by their respective temperatures $T_{i,e}$ and corresponding adiabatic indices $\Gamma_{i,e}$,

$$p_{i,e\text{th}} = n_{i,e\text{th}} k_B T_{i,e}, \quad (6)$$

$$u_{i,e\text{th}} = \frac{p_{i,e\text{th}}}{\Gamma_{i,e}(\theta_{i,e}) - 1}. \quad (7)$$

For each species, the adiabatic index $\Gamma(\theta)$ is a function of temperature through the dimensionless ratio $\theta = k_B T / m c^2$, transitioning from $\Gamma = 5/3$ for non-relativistic particles ($\theta \ll 1$) to $\Gamma = 4/3$ for relativistic particles ($\theta \gg 1$).

Instead of directly tracking the temperatures or energy densities of the individual species, we work with the electron and ion entropy per particle $s_{i,e}$, which allows us to break up the evolution into adiabatic and non-adiabatic steps. For a non-degenerate relativistic gas, there exist exact closed form expressions for the adiabatic index $\Gamma(\theta)$ and the entropy per particle $s(\theta, n)$ (Chandrasekhar 1939). However, because the exact expressions involve computationally expensive Bessel functions and are not easy to invert, we use approximate forms. Our approach is based on a fitting function to the specific heat at constant volume, which we can integrate to find expressions for the internal energy, (see Appendix A of Sądowski et al. 2017)¹

$$\frac{u(\theta)}{p(\theta)} = \frac{1}{\Gamma(\theta) - 1} = 3 - \frac{3}{5\theta} \ln \left[1 + \frac{5\theta}{2} \right], \quad (8)$$

and the entropy per particle,

$$s = k_B \ln \left[\frac{\theta^{3/2} (\theta + 2/5)^{3/2}}{n} \right]. \quad (9)$$

We assume that nonthermal particles are isotropic in

¹ Sądowski et al. 2017 derived equation (8) in Appendix A, but used a simpler fitting function for $u(\theta)$ to enable direct inversion to solve for θ . Here we have chosen to use equation (8) in order to maintain consistency in our approximations, though at a small additional computational cost. On the occasions that we need to solve for θ from u , we use a Newton-Raphson solver to invert equation (8), which converges rapidly.

the fluid rest frame, with a distribution $n(\gamma)$ in Lorentz factor γ . In the current work, we consider $n(\gamma)$ over a range of γ from a minimum γ_{min} to a maximum γ_{max} . The number density, energy density, and pressure of the nonthermal electrons are then simply given by integrals over the distribution $n(\gamma)$,

$$n_{e\text{nth}} = \int_{\gamma_{\text{min}}}^{\gamma_{\text{max}}} n(\gamma) d\gamma, \quad (10)$$

$$u_{e\text{nth}} = m_e c^2 \int_{\gamma_{\text{min}}}^{\gamma_{\text{max}}} n(\gamma) (\gamma - 1) d\gamma, \quad (11)$$

$$p_{e\text{nth}} = \frac{m_e c^2}{3} \int_{\gamma_{\text{min}}}^{\gamma_{\text{max}}} n(\gamma) (\gamma - \gamma^{-1}) d\gamma, \quad (12)$$

where m_e is the electron mass.²

When necessary, we calculate the net adiabatic index of the combined three-species fluid directly,

$$\Gamma_{\text{int}} = 1 + \frac{p}{u} = 1 + \frac{p_i + p_{e\text{th}} + p_{e\text{nth}}}{u_i + u_{e\text{th}} + u_{e\text{nth}}}, \quad (13)$$

using equations (6–8) for the thermal quantities and equations (11) and (12) for the nonthermal energy and pressure.

2.2 Radiation

In addition to the three fluid components described above, we concurrently evolve an independent fluid to represent radiation. We specify the radiation field using the M1 closure scheme (Levermore 1984), as described in Sądowski et al. (2013, 2014); McKinney et al. (2014). In effect we assume that, at each spacetime point, there exists a ‘radiation frame’ in which the radiation is isotropic. Thus the frequency-integrated radiation field is described by its energy density \bar{E} in the radiation frame and the timelike four velocity $u_r^\mu \neq u^\mu$ of this frame (the evolution equations which determine the radiation frame four-velocity are described in Section 2.6). In an arbitrary frame, the radiation stress energy tensor then takes the form

$$R^\mu{}_\nu = \frac{4}{3} \bar{E}_r u_r^\mu u_{r\nu} + \frac{1}{3} \bar{E}_r \delta^\mu{}_\nu. \quad (14)$$

Throughout this work, quantities in the radiation rest frame are denoted with bars, and quantities in the fluid frame are denoted with hats. In particular, while \bar{E} is the radiation energy density evolved by the code, the fluid frame quantity \hat{E} is what enters into the equations describing the interactions between radiation and the fluid components.

We also independently evolve the radiation frame photon number \bar{n}_r , which is useful for calculating the radiation temperature. Under the assumption that the radiation spectrum is a grey body (Sądowski & Narayan 2015), the radiation temperature in the fluid frame is

$$T_r = \frac{\hat{E}}{2.7012 k_B \hat{n}_r}, \quad (15)$$

where \hat{E} and \hat{n}_r are the radiation energy density and photon number transformed to the fluid frame.

² The $m_e c^2 (\gamma - \gamma^{-1}) / 3$ factor in the integrand for the pressure $p_{e\text{nth}}$ is just $p^2 / 3E$, where $p^2 = m_e c^2 (\gamma^2 - 1)$ is the square of the particle momentum, $E = \gamma m_e c^2$ is the particle energy, and the $1/E$ factor comes from the relativistically invariant measure $d^3\mathbf{p}/E$ (e.g. Mihalas & Mihalas 1984).

2.3 GRRMHD equations

The conservation equations that govern the evolution of the fluid, magnetic field, and radiation field are

$$(\rho u^\mu)_{;\mu} = 0, \quad (16)$$

$$T^\mu_{\nu;\mu} = G_\nu, \quad (17)$$

$$R^\mu_{\nu;\mu} = -G_\nu, \quad (18)$$

$$F^{*\mu}_{\nu;\mu} = 0. \quad (19)$$

Here, $F^{*\mu\nu} = b^\mu u^\nu - b^\nu u^\mu$ is the dual of the MHD Maxwell tensor, and G_ν is the four-force density that couples the evolution of the radiation and gas (see equation 20 and 21). We assume that both the thermal and nonthermal electrons radiate isotropically in the fluid rest frame. Hence, the total energy-momentum flux from radiation to the gas is

$$\hat{G}^0 = \tilde{\rho}(\kappa_{P,a}\hat{E} - 4\pi\kappa_{P,e}\hat{B}) + \hat{G}_{IC\text{ th}}^0 + \hat{G}_{\text{nth}}^0, \quad (20)$$

$$\hat{G}^i = (\tilde{\rho}\kappa_R + \rho\kappa_{es})\hat{F}^i. \quad (21)$$

In these equations, the κ factors are the total, frequency-averaged opacities for the thermal radiative processes; the distinctions between the different factors are explained below. $\hat{G}_{IC\text{ th}}^0$ is the thermal energy loss from inverse Compton scattering, and \hat{G}_{nth}^0 is the energy loss to radiation from the nonthermal population. $\tilde{\rho}$ is the fluid density reduced to account for the nonthermal population (see below), \hat{F}^i is the radiation momentum flux, and $\hat{B} = \sigma T_e^4/\pi$ is the electron blackbody radiance.

We ignore absorption by the nonthermal population (Section 2.4). Therefore, in the rest frame, the nonthermal population only contributes an emission factor to the energy term \hat{G}_{nth}^0 . The contribution to the radiative power from the nonthermal electrons is the integral of the radiative cooling rate over the distribution,

$$\hat{G}_{\text{nth}}^0 = m_e c^2 \int_{\gamma_{\text{min}}}^{\gamma_{\text{max}}} n(\gamma) \dot{\gamma}_{\text{rad}} d\gamma. \quad (22)$$

The quantity $\dot{\gamma}_{\text{rad}}$ represents the cooling rate of an electron with energy $\gamma m_e c^2$ from radiative processes in the fluid rest frame; it is always negative. The total radiative cooling rate has contributions from synchrotron, bremsstrahlung, and inverse Compton scattering,

$$\dot{\gamma}_{\text{rad}} = \dot{\gamma}_{\text{syn}} + \dot{\gamma}_{\text{brem}} + \dot{\gamma}_{IC}, \quad (23)$$

where $\dot{\gamma}_{\text{syn}}$, $\dot{\gamma}_{\text{brem}}$, $\dot{\gamma}_{IC}$ are given by equations (31, 32, 33), respectively.

The thermal electrons contribute an emission term $4\pi\tilde{\rho}\kappa_{P,e}\hat{B}$ and an absorption term $\tilde{\rho}\kappa_{P,a}\hat{E}$ to the energy flux. Because we ignore absorption by the nonthermal electrons, the momentum flux comes entirely from the thermal absorption term $\tilde{\rho}\kappa_R\hat{F}^i$ and the electron scattering term $\rho\kappa_{es}\hat{F}^i$, where \hat{F}^i is the radiation flux in the fluid frame.

We use frequency-averaged, grey opacities for thermal synchrotron and bremsstrahlung emission. Following the suggestion of Mihalas & Mihalas (1984), we use the Planck averaged mean opacities $\kappa_{P,e}$ and $\kappa_{P,a}$ weighted for emission and absorption in the energy equation (\hat{G}^0), and we use the Rosseland mean opacity κ_R in the momentum equation (\hat{G}^i). The full expressions for these opacities as a function of number density and temperature are given in Sądowski et al. (2017). The electron scattering opacity is κ_{es} ; it includes a

Klein-Nishina factor that lowers the scattering cross section at high photon energies (Buchler & Yueh 1976),

$$\rho\kappa_{es} = (n_{e\text{ th}} + n_{e\text{ nth}})\sigma_T \left[1 + \frac{T_r}{4.5 \times 10^8 \text{ K}} \right]^{0.86} \text{ cm}^{-1}. \quad (24)$$

Note that the density multiplying most of the thermal synchrotron and bremsstrahlung opacities in equations (20) and (21) is $\tilde{\rho}$, which corresponds to thermal electrons alone,

$$\tilde{\rho} = \rho \frac{n_{e,\text{th}}}{n_{e,\text{th}} + n_{e\text{ nth}}}. \quad (25)$$

The full density ρ is used for the electron scattering opacity, since the nonthermal electrons also scatter the emission.

Finally, inverse Compton scattering off of thermal electrons contributes the last term, $\hat{G}_{IC\text{ th}}^0$. The full expression for $\hat{G}_{IC\text{ th}}^0$ can be found in Sądowski & Narayan (2015).

2.4 Nonthermal population evolution equation

The evolution equation for the nonthermal distribution can be derived by taking angular moments of the relativistic Boltzmann equation and imposing the requirement that the distribution be isotropic in the fluid rest frame (Lindquist 1966; Webb 1985, 1989). The isotropy assumption truncates the hierarchy of moment equations and leaves a single equation,

$$[n(\gamma)u^\alpha]_{;\alpha} = -\frac{\partial}{\partial\gamma} [\dot{\gamma}_{\text{tot}}n(\gamma)] + Q_I(\gamma), \quad (26)$$

$$\dot{\gamma}_{\text{tot}} = \dot{\gamma}_{\text{adiab}} + \dot{\gamma}_C + \dot{\gamma}_{\text{rad}}. \quad (27)$$

Aside from the injection (source) term $Q_I(\gamma)$, equation (26) is essentially a conservation equation in five dimensions: four dimensions correspond to space and time (left-hand side of equation 26), and the fifth dimension corresponds to the fluid frame particle Lorentz factor γ , through which particles move with velocity $\dot{\gamma}_{\text{tot}}$. This velocity is broken into three parts: $\dot{\gamma}_{\text{adiab}}$ from adiabatic heating and cooling due to gas compression and expansion, $\dot{\gamma}_C$ from cooling due to the (weak) Coulomb coupling with the thermal electrons, and $\dot{\gamma}_{\text{rad}}$ from the energy lost to radiation (equation 23). Since we assume nonthermal electrons only emit and do not absorb, $\dot{\gamma}_{\text{rad}}$ is always negative; furthermore, the Coulomb coupling term $\dot{\gamma}_C$ is also negative, since the nonthermal population by assumption consists of particles more energetic than the thermal electrons that they couple to.

The adiabatic ‘cooling’ rate $\dot{\gamma}_{\text{adiab}}$ can be positive or negative, depending on whether the gas is compressing or expanding. This term can be derived from the relativistic Boltzmann equation without interaction terms (Webb 1989),

$$\dot{\gamma}_{\text{adiab}} = -\frac{1}{3}u^\alpha_{;\alpha}(\gamma - \gamma^{-1}). \quad (28)$$

It is negative when the gas expands, $\equiv u^\alpha_{;\alpha} > 0$, and it is positive when the gas is compressing.

The term $Q_I(\gamma)$ in equation (26) is the rate of injection of high energy electrons from the thermal to the nonthermal distribution at a given γ . In principle, $Q_I(\gamma)$ is a function of local conditions and depends on microscopic plasma processes that accelerate electrons into the nonthermal distribution. For simplicity, in this study, we assume that the electrons are injected with a power-law distribution with a

constant index p ,

$$Q_I(\gamma) = C\gamma^{-p}. \quad (29)$$

In addition, we assume that the total rate of energy injection into the high energy population is a fixed fraction δ_{nth} of the total electron viscous heating rate $\delta_e q^v$. This determines the normalization C in equation (29),

$$m_e c^2 \int (\gamma - 1) Q_I(\gamma) = \delta_{\text{nth}} \delta_e q^v. \quad (30)$$

Thus, given the total viscous heating rate q^v , which we compute numerically from the simulation (see equation 48), we add a fraction δ_e of the energy to the electrons, of which a fraction δ_{nth} goes into the nonthermal population. These heating fractions are adjustable parameters of the model; in this work, we follow Ressler et al. (2015) and Sądowski et al. (2017) in using the fitting formula of Howes (2010) to determine δ_e as a function of species temperature and plasma magnetization, and we set δ_{nth} equal to a constant value ($\delta_{\text{nth}} = 0.015$ for the nonthermal run described in Section 5).

Apart from $\dot{\gamma}_{\text{adiab}}$, the model includes additional cooling rates, $\dot{\gamma}_{\text{syn}}$, $\dot{\gamma}_{\text{brem}}$, $\dot{\gamma}_{\text{IC}}$, $\dot{\gamma}_{\text{C}}$, for synchrotron, bremsstrahlung, inverse Compton scattering, and Coulomb coupling. We use expressions from Manolakou et al. (2007) and Ginzburg & Syrovatskii (1964), valid in the relativistic limit ($\gamma \gg 1$),

$$\dot{\gamma}_{\text{syn}} = -1.292 \times 10^{-11} \left(\frac{B}{1 \text{ G}} \right)^2 \gamma^2 \text{ s}^{-1}, \quad (31)$$

$$\dot{\gamma}_{\text{brem}} = -1.37 \times 10^{-16} \left(\frac{n_i}{1 \text{ cm}^{-3}} \right) \gamma (\ln \gamma + 0.36) \text{ s}^{-1}, \quad (32)$$

$$\dot{\gamma}_{\text{IC}} = -3.25 \times 10^{-8} \left(\frac{\hat{E}}{1 \text{ erg cm}^{-3}} \right) \gamma^2 F_{KN}(\gamma) \text{ s}^{-1}, \quad (33)$$

$$\dot{\gamma}_{\text{C}} = -1.491 \times 10^{-14} \left(\frac{n_{e \text{ th}}}{1 \text{ cm}^{-3}} \right) \times \left[\ln \gamma + \ln \left(\frac{n_{e \text{ th}}}{1 \text{ cm}^{-3}} \right) + 74.7 \right] \text{ s}^{-1}. \quad (34)$$

The inverse Compton cooling rate $\dot{\gamma}_{\text{IC}}$ includes a dimensionless Klein-Nishina factor F_{KN} which reduces the cooling rate at high γ . For a thermal distribution of photons at temperature T_r , this factor is (Manolakou et al. 2007; Moderski et al. 2005)

$$F_{KN}(\gamma) = \left(1 + 11.2\gamma \frac{kT_r}{m_e c^2} \right)^{-3/2}. \quad (35)$$

2.5 Thermal population evolution

The evolution of the thermal ions and electrons is handled as in Sądowski et al. (2017), with additional terms to describe the new interactions with nonthermal electrons. For both species, the thermal entropy per particle evolves according to the first law of thermodynamics,

$$T_e (n_{e \text{ th}} s_e u^\mu)_{;\mu} = \delta_e (1 - \delta_{\text{nth}}) q^v + q_{\text{th}}^C + \hat{G}_{\text{th}}^0, \quad (36)$$

$$+ q_{\text{nth}}^C + \left(q^{\text{cool}} - \mu \dot{n}^{\text{cool}} \right),$$

$$T_i (n_i s_i u^\mu)_{;\mu} = (1 - \delta_e) q^v - q_{\text{th}}^C. \quad (37)$$

The first term on the right-hand side in both equations represents the viscous heating of the thermal populations. The

total viscous heating rate q^v is identified numerically in our algorithm, as described later (see equation 48). The fraction of the viscous heating that goes to the thermal ions is $(1 - \delta_e)$, and the fraction that goes into thermal electrons is $(1 - \delta_{\text{nth}}) \delta_e$. The second term in both equations is the thermal Coulomb coupling q_{th}^C between the thermal electron and ion populations; the expression we use is from Stepney & Guilbert (1983), and can be found in Sądowski et al. (2017). The third term in the electron entropy equation is the net emission and absorption of energy from radiation, \hat{G}_{th}^0 (equation 20).

The nonthermal population modifies the electron entropy evolution through a Coulomb coupling term q_{nth}^C , which is the total energy gained by the thermal electrons due to the Coulomb cooling of the high-energy particles,

$$q_{\text{nth}}^C = -m_e c^2 \int n(\gamma) \dot{\gamma}_{\text{C}} d\gamma. \quad (38)$$

Finally, in order to conserve the total number of electrons, we assume that when nonthermal electrons cool below γ_{min} , they are thermalised and join the thermal distribution. These cooling electrons join the thermal distribution at a rate \dot{n}^{cool} , carrying energy density q^{cool} . The expression $\mu \dot{n}^{\text{cool}}$, where μ is the chemical potential, accounts for the increase in entropy from the increase in particle number density. The energy and particle cooling rates from the nonthermal distribution to the thermal distribution are simply the flux of energy and particles at the boundary γ_{min} ,

$$\dot{n}^{\text{cool}} = -[\dot{\gamma}_{\text{tot}} n(\gamma)]_{\gamma_{\text{min}}},$$

$$q^{\text{cool}} = -[m_e \dot{\gamma}_{\text{tot}} (\gamma - 1) n(\gamma)]_{\gamma_{\text{min}}}. \quad (39)$$

Note that during adiabatic compression, there can be a (small) flux out of the nonthermal distribution at γ_{max} ; we treat this similarly, adding back the energy and particle number lost over this edge to the local thermal bath. This treatment is unphysical but necessary to conserve energy among the three species in the simulation. Since the total amount of viscous heating is not increased by this procedure (see equation (48)), this choice will not increase the temperature of the thermal electron population above what it would be in a simulation without any nonthermal electrons. In any case, due to the steep power-law shape of the injection functions considered in this study (equation (29)), the outward flux at γ_{max} is always extremely small.

For the chemical potential μ , we use the following expression derived from our approximate form of the entropy, equation (9),

$$\mu = m_e c^2 \left[1 - \frac{3}{5} \ln \left(1 + \frac{5}{2} \theta_e \right) + \theta_e \left(4 - \frac{3}{2} \ln \left(\theta_e^2 + \frac{2}{5} \theta_e \right) + \ln n_{e \text{ th}} \right) \right]. \quad (40)$$

2.6 Radiation evolution

The evolution of the radiation energy density \bar{E} and the radiation frame velocity u_r is determined by the coupled GRMHD equations (16)–(19). Evolving the photon number density requires a separate equation (Sądowski et al. 2015),

$$(\bar{n}_r u_r^\mu)_{;\mu} = \hat{n}_r, \quad (41)$$

where \hat{n}_r is the frame-invariant photon production rate (Sądowski & Narayan 2015),

$$\hat{n}_r = \hat{n}_{r,\text{syn}} + \hat{n}_{\text{brem,th}} + \hat{n}_{\text{brem,nth}} - \tilde{\rho}\kappa_{n,a}\hat{n}_r. \quad (42)$$

The first term in equation (42) is from synchrotron emission of both thermal and nonthermal electrons (the number of photons emitted in synchrotron is independent of the energy of the emitting particle),

$$\hat{n}_{r,\text{syn}} = 1.46 \times 10^5 \left(\frac{B}{1 \text{ G}} \right) (n_{e,\text{th}} + n_{e,\text{n}}). \quad (43)$$

The second term is the production of photons from thermal bremsstrahlung emission (see Sądowski et al. 2017). The third term gives the corresponding rate of photon emission by bremsstrahlung from the nonthermal distribution. For an electron at γ , we approximate the bremsstrahlung photon production by assuming that photons are only produced with energy $h\nu = \gamma m_e c^2$,

$$\hat{n}_{\text{brem,nth}} = \int_{\gamma_{\text{min}}}^{\gamma_{\text{max}}} \frac{\hat{\gamma}_{\text{brem}}}{\gamma} n(\gamma) d\gamma. \quad (44)$$

Finally, the last term is the photon loss rate from absorption by the thermal electrons, which can be written in terms of a number absorption opacity $\kappa_{n,a}$ (see Sądowski et al. 2017).

3 NUMERICAL METHODS

We have implemented the equations in Section 2 in the GRRMHD code KORAL (Sądowski et al. 2013, 2014, 2017). The nonthermal electron distribution $n(\gamma)$ is sampled in N equally spaced logarithmic bins over a range $[\gamma_{\text{min}}, \gamma_{\text{max}}]$. These quantities $n(\gamma_j)$ are N additional primitive quantities which we evolve in parallel with the remaining GRRMHD and thermodynamic primitives. The full vector of primitives P_i consists of the fluid density ρ , energy density u , fluid velocity u^i ; the magnetic field B^i , radiation energy density \bar{E} , radiation frame velocity u_r^i ; the photon number n_r , thermal electron and ion entropy densities $s_e n_{e,\text{th}}$ and $s_i n_i$; and the populations $n(\gamma_j)$ of the nonthermal electrons:

$$P = [\rho, u, u^i, B^i, \bar{E}, u_r^i, n_r, s_e n_{e,\text{th}}, s_e n_i, n(\gamma_j)], \quad (45)$$

where the index j runs over the N bins sampled in γ -space. The corresponding conserved quantities are

$$U = [\rho u^0, T_0^0 + \rho u^0, T_i^0, B^i, R_0^0, R_i^0, n_r u^0, s_e n_{e,\text{th}} u^0, s_e n_i u^0, n(\gamma_j) u^0]. \quad (46)$$

The code uses a Newton-Raphson solver to convert from the conserved quantities to primitives (Sądowski et al. 2013, 2014). Since the fluid velocity u^μ is uniquely specified by inverting the MHD conserved quantities, to recover $n(\gamma_j)$ we simply divide the conserved quantity $n(\gamma_j)u^0$ by u^0 after the Newton-Raphson solver has found a solution for the MHD and radiation primitives.

Fixed floors and ceilings are applied on the evolved quantities as in Sądowski et al. (2013, 2014, 2017). We impose an absolute floor on the nonthermal distribution $n(\gamma_j) > 0$. This is especially necessary when beginning from $n(\gamma_j) = 0$, as numerical effects can occasionally make q^v negative and bring the nonthermal number values below

zero. We also impose fixed ceilings to prevent the nonthermal number and energy densities from exceeding 50 per cent of the total.

KORAL uses a second-order Runge-Kutta scheme to advance the fluid quantities in each time step. Within each Runge-Kutta step, there are three main substeps: explicit fluid evolution (Section 3.1), nonthermal adiabatic evolution and viscous heating (Section 3.2), and implicit radiation and Coulomb coupling (Section 3.3).

3.1 Explicit fluid evolution

In the explicit substep, the covariant conservation equations are evolved without source terms.

The equations evolved are the GRRMHD equations, equations (16–19), the photon number equation (41), the thermal entropy equation (36), and the nonthermal advection equation (26), all with their right hand sides set to zero. In particular, we treat the nonthermal distribution at each point in γ -space independently and evolve these variables with the spatial fluid flow. The explicit evolution uses a Lax-Friedrichs method with van-Leer flux limiters to calculate fluxes of the conserved quantities at cell faces. Geometrical terms (i.e. the covariant derivative terms involving Christoffel symbols) are added as source terms at cell centres. The full explicit advective algorithm is described in Sądowski et al. (2013, 2014).

Physically, entropy density is not exactly conserved on a finite grid, despite the form of equation (36). When we bring two (same-species) finite gas parcels together and mix them to an equilibrium energy and temperature, the total energy density is constant, but entropy increases. If we solve the source-free version of equation (36) with finite-volume methods, the entropy will be preserved exactly, and the final energy density will be underestimated, causing the viscous heating identified in the next step to be systematically too large.

To avoid this problem, we adopt the simple solution from Sądowski et al. (2017) of mixing the entropies from neighboring cells at constant density.³ In the explicit evolution of the adiabatic entropy equation, we identify the initial values of the entropy flux on each of the cell walls, as well as the mixing fractions which they contribute to the total entropy increase in the cell over the time step. We then take these same mixing fractions and uses them to instead add up the energy densities computed from the boundary entropy fluxes, keeping the fluid density fixed. Once we have the species energy increase, we invert (using equations 8 and 9) to find the final value of the entropy. This approach is computationally convenient and limits excess viscous heating.

3.2 Adiabatic Nonthermal Evolution and Viscous Heating

After evolving the bulk fluid quantities explicitly, we evolve the nonthermal distribution in each cell adiabatically through γ -space to provide the appropriate heating or cooling from gas compression or expansion. Then we calculate

³ As noted there, mixing at constant pressure may be a more consistent procedure.

the total energy dissipated and apply it to the thermal and nonthermal species using our viscous heating prescription. The steps are as follows:

(i) The nonthermal distribution is evolved under adiabatic compression/expansion using the cooling rate $\dot{\gamma}_{\text{adiab}}$ in equation (28). From equation (26), after explicit spatial evolution and before dealing with radiative and Coulomb coupling, the change in the nonthermal electron spectrum $n(\gamma_j)$ over a proper time interval $\Delta\tau$ at each bin j in γ -space is

$$\Delta n(\gamma_j) = \Delta\tau \left(\frac{u_{;\alpha}^\alpha}{3} \right) \left[\frac{\partial}{\partial\gamma} ((\gamma - \gamma^{-1})n(\gamma)) \right]_j. \quad (47)$$

The expansion parameter $u_{;\alpha}^\alpha$ is computed from the u^α obtained at the end of the explicit operator. For numerical stability, the derivative $\partial/\partial\gamma$ is approximated using explicit upwind finite differencing. The upwind direction depends on the sign of the expansion.

Because the upwind evolution in equation (47) conserves total particle number but not energy, the spectrum $\Delta n(\gamma)$ of particles added or subtracted to the distribution is scaled so that the total change in energy is equal to the amount predicted by equation (49) (see Section 3.4).

(ii) If the expansion $u_{;\alpha}^\alpha > 0$, nonthermal electrons may escape out of the lowest bin of the distribution. The loss of energy and particles out of the lowest bin is calculated and added to the thermal distribution number and energy density. Similarly, if $u_{;\alpha}^\alpha < 0$, nonthermal electrons may escape out of the highest bin, and the corresponding flux of energy and number density is added to the thermal distribution. The thermal electron entropy per particle s_e is recomputed using the updated number and energy density.

(iii) Since each species has now gone through its full adiabatic evolution, we calculate the viscous dissipation rate q^v in each cell by comparing the total fluid energy density after the explicit step with the sum of the current species energies (Sądowski et al. 2017),

$$q^v = \frac{1}{\Delta\tau} (u - u_{i \text{ th adiab}} - u_{e \text{ th adiab}} - u_{e \text{ nth adiab}}). \quad (48)$$

Here, u is the internal energy density of the total gas after the explicit step over a fluid frame proper time step $\Delta\tau$. $u_{i \text{ th adiab}}$, $u_{e \text{ th adiab}}$, and $u_{e \text{ nth adiab}}$ are the internal energy densities carried by thermal ions, electrons, and nonthermal electrons after adiabatic evolution. The difference between u and the sum of the adiabatically evolved species energy densities gives the total energy gained from viscous dissipation during the time step.

(iv) The fraction of the viscous heating applied to the electrons δ_e , and the fraction of that applied to the nonthermal population δ_{nth} are calculated depending on the prescription used.

(v) Particles are added to the nonthermal population in a power-law distribution by adding the quantity in equation (29) to each bin.

(vi) The thermal energy densities $u_{e, \text{th}}$ and u_i are increased by their fraction of the remaining viscous heating. The corresponding changes in thermal entropies s_e and s_i are computed by equations (8–9).

3.3 Implicit Radiation and Coulomb Coupling

The source terms representing the radiative and Coulomb coupling between the species are: the radiative coupling G_ν , the thermal Coulomb coupling q_{th}^C , the photon source term \dot{n}_r , the nonthermal cooling rates $\dot{\gamma}$, the nonthermal Coulomb coupling q_{nth}^C , and the cooling from the nonthermal population to the thermal bath, q^{cool} and $\mu\dot{n}^{\text{cool}}$. These coupling terms in equations (16), (36) and (26) are applied through a semi-implicit operator using the methods described in Sądowski et al. (2013, 2014).

The implicit solver uses a reduced set of primitives which includes the energy density and velocity of *either* gas or radiation, the photon number density, electron energy density, and the full nonthermal distribution. The other primitives, including the velocity not evolved, the gas density, and the ion entropy are continually updated during the iterations of the implicit solver to enforce the appropriate conservation laws.

3.4 Energy vs Particle Conservation

The equation that governs the evolution of the nonthermal distribution, equation (26), is a conservation law for a particle current in five dimensions, three spatial, one time, and one corresponding to the individual particle energies. As this equation is evolved via our finite volume algorithms (and as we account properly for the loss of particles at γ_{min} and γ_{max}), the total number of particles in the distribution is conserved. The total internal energy density in the distribution is given by integrating $n(\gamma)$ times the particle energy $(\gamma-1)m_e c^2$ over γ (equation 11). While particles are not lost from the distribution (excepting boundary effects), energy can be lost in radiative cooling, Coulomb coupling, or adiabatic expansion; it can be gained in adiabatic compression. Because the finite volume form of equation (26) does not conserve the particle energy current, and because we use a numerical approximation to the integral in equation (11) to compute the internal energy in the nonthermal distribution, the evolution of the nonthermal distribution on its own does not conserve energy.

We account for this in two ways. In the implicit step, where nonthermal electrons lose energy to radiation and Coulomb coupling, we simply ensure that overall energy is conserved by adjusting the nonthermal energy flux into radiation ($-\dot{G}_{\text{nth}}^0$) to reflect the energy that is actually lost in cooling the nonthermal distribution. That is, instead of using equation (22), we compute \dot{G}_{nth}^0 by computing the difference in the total nonthermal energy density at a given substep in the implicit solver with the energy density computed before the implicit step, subtracting off the small part of the cooling that is due to Coulomb coupling (which goes into thermal electrons). When we need to compute \dot{G}_{nth}^0 outside of the implicit solver, we use equation (22). In this way, the total energy is conserved and the shape of the nonthermal distribution is not affected, although the total energy in the distribution may differ from the value computed from an analytic solution or found in a simulation with finer sampling in γ .

In the intermediate step, where particles are heated or cooled by adiabatic compression or expansion, we cannot account for the missing/extra energy by simply adding it to

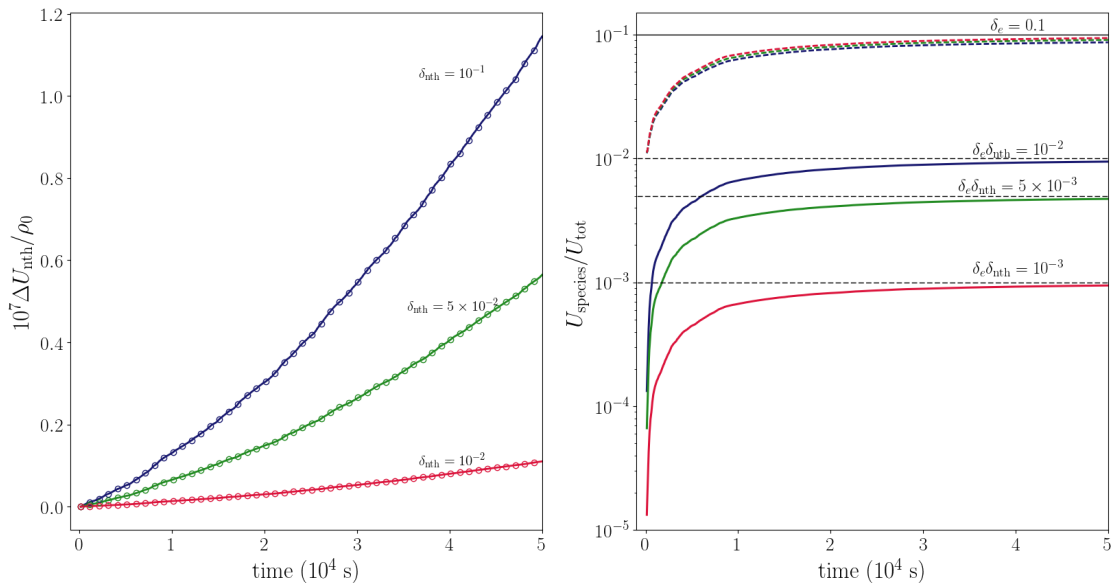


Figure 1. (Left) The increase of the total energy of nonthermal electrons ΔU_{nth} integrated over the turbulent box of Section 4.1. The total electron heating fraction was set at $\delta_e = 0.1$, and three runs were performed with nonthermal heating fraction $\delta_{\text{nth}} = 0.01$ (red), $\delta_{\text{nth}} = 0.05$ (green), and $\delta_{\text{nth}} = 0.1$ (blue). The open circles indicate the increase of the internal energy of the nonthermal population, and the solid lines show the predicted increase, which is the fraction $(\delta_e \delta_{\text{nth}})$ of the increase in the total gas energy. (Right) The fraction $U_{\text{species}}/U_{\text{tot}}$ of thermal electrons (dashed lines) and nonthermal electrons (solid lines). As time proceeds and energy from viscous dissipation is divided among the different species, the energy fraction in each species asymptotes to the value given by the corresponding fixed viscous heating injection fractions: $\delta_e(1 - \delta_{\text{nth}})$ for thermal electrons, and $\delta_e \delta_{\text{nth}}$ for nonthermal electrons.

radiation or the thermal population. This is because the adiabatic heating/cooling of the nonthermal distribution is part of the adiabatic evolution, and correctly computing the viscous heating via equation (48) depends on properly evolving the independent species energies adiabatically. In this case, we evolve the distribution explicitly, and then scale the computed $\Delta n(\gamma_j)$ at each sampled γ_j so that the total change in energy is equal to the amount given by the total instantaneous rate of energy increase,

$$\Delta u = m_e c^2 \int \dot{\gamma}_{\text{adiab}} n(\gamma) d\gamma. \quad (49)$$

Scaling the distribution in this way can bias the shape of the distribution (Section 4.2). However, the energy gained and lost in this step is applied correctly (Section 4.1), and the computation of the viscous heating rate q^v is consequently not biased.

4 TESTS

In this section we describe several test problems to demonstrate the accuracy of the nonthermal electron evolution as implemented in KORAL. In Section 4.1, we test the bulk heating of the nonthermal electrons in a turbulent box. In Section 4.2 we compute the evolution of the electron distribution under constant injection and adiabatic compression, and in Section 4.3 we test evolution from injection, synchrotron cooling, and inverse Compton scattering. We compare the numerical results with analytic and semi-analytic solutions to gauge the accuracy of the algorithms.

4.1 Driven Turbulence

To test the implementation of adiabatic evolution and viscous heating of the nonthermal population, we repeated the turbulent box test from Sądowski et al. (2017), which was inspired by the MHD driven turbulence test of Ressler et al. (2015). A fraction $\delta_e = 0.1$ of the dissipative heating q^v is deposited into the electrons, of which a fraction δ_{nth} goes into the nonthermal population via equation (29), with the remaining fraction $\delta_e(1 - \delta_{\text{nth}})$ going into the thermal electrons by equation (36).

We start with an initial uniform two dimensional system of size L with density ρ_0 , zero velocity, speed of sound $c_{s0} = 8.6 \times 10^{-4}c$, a horizontal magnetic field with $\beta = p_{\text{gas}}/p_{\text{mag}} = 6$, no nonthermal electrons, and periodic boundary conditions. We drive the system with random, divergence-free Gaussian perturbations in the velocity with a power spectrum $P(|\delta v|^2) = k^6 \exp(-8k/k_{\text{pk}})$, where $k_{\text{pk}} = 4\pi/L$. These perturbations add kinetic energy to the system which dissipates into internal energy of the gas, divided among the three species. Radiation and Coulomb coupling are turned off.

The open circles in the left panel of Fig. 1 shows the resulting increase of the total energy in nonthermal electrons integrated over the simulation volume for three runs with $\delta_{\text{nth}} = .01, .05, \text{ and } .1$, respectively (open circles). The circles are compared with the corresponding fraction $\delta_e \delta_{\text{nth}}$ of the increase in the total gas energy (solid lines). The close agreement shows that the combination of viscous heating and the net change in energy from adiabatic compression

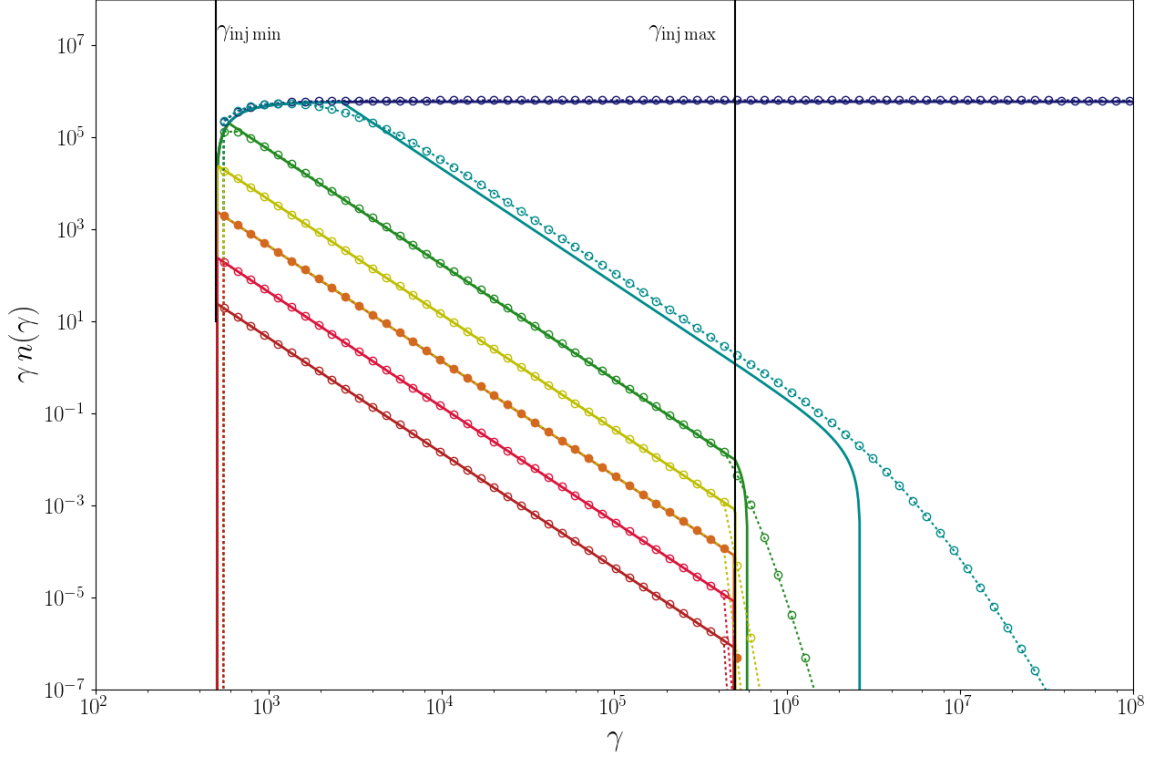


Figure 2. Results of a test of adiabatic compression with constant $u_{;\mu}^{\mu} = -5 \times 10^{-3} \text{ s}^{-1}$ and particle injection with slope $p = 3.5$ between $\gamma_{\text{inj min}} = 50$ and $\gamma_{\text{inj max}} = 5 \times 10^5$. The injection distribution is normalized so that the total injection rate is $1000 \text{ cm}^{-3} \text{ s}^{-1}$. The solid lines show the analytic solution to the problem at times (from below) $t = 10^{-2}, 10^{-1}, 1, 10, 10^2, 10^3$ and 10^4 seconds. The open circles show the KORAL solution at the corresponding times.

and expansion (as a result of turbulence) is handled correctly. In particular, the energy normalization performed on the nonthermal distribution during the adiabatic compression/expansion step (Section 3.4) is necessary to identify the correct amount of viscous heating and produce the good agreement shown in Fig. 1.

The right panel of Fig. 1 shows the ratio of the energy densities of the two electron populations to the total gas energy density: $U_{\text{th}}/U_{\text{gas}}$, and $U_{\text{nth}}/U_{\text{gas}}$. As energy is dissipated and divided among the species, the ratios of the species energies to the total internal energy correctly asymptote to the injection fractions $\delta_e(1 - \delta_{\text{nth}})$ and $\delta_e\delta_{\text{nth}}$ for thermal and nonthermal electrons, respectively.

4.2 Particle Injection and Adiabatic Compression

To test the implementation of the adiabatic heating and cooling of electrons under gas compression and expansion (equation 28), we consider a zero-velocity gas background with constant injection of nonthermal electrons with a power-law slope $p = 3.5$ between $\gamma_{\text{inj min}} = 50$ and $\gamma_{\text{inj max}} = 5 \times 10^5$. We also subject the system to a constant artificial compression rate (not computed from the actual gas four-velocity) $u_{;\mu}^{\mu} = -5 \times 10^{-3} \text{ s}^{-1}$, similar to the compression rate found in the equatorial plane at a ra-

dius of $\sim 5 r_g$ in the accretion disc simulations described later in Section 5. We turn off the radiative and Coulomb coupling interactions. The analytic solution to this problem (Manolakou et al. 2007, Appendix A) shows the development of a break from the injection power-law slope $-p$ to a slope of -1 at low γ , with the break propagating to higher γ with increasing time.

Fig. 2 shows the results of the test at logarithmically spaced time intervals. The open circles, which denote the KORAL solution, mostly line up well with the analytic result. Deviations arise from two effects. First, the numerical scheme is diffusive and thus smooths out sudden breaks in the slope of $n(\gamma)$. This is seen as a tail above the maximum γ of the true distribution, and also at the break between slope -3.5 to -1 , around $\gamma = 3000$ for $t = 1000 \text{ s}$. Second, the smoothing out of breaks leads to a loss of energy from the analytic value. Since we conserve the total energy, this leads to a shift in the normalization (Section 3.4). This effect is obvious in the KORAL solution at $t = 10^3 \text{ s}$. Once the spectrum has broken completely, the KORAL solution matches the analytic solution for all γ . In practice, fluid in a turbulent simulation will experience many phases of compression and expansion, which should wash out the energy correction effect illustrated in this test.

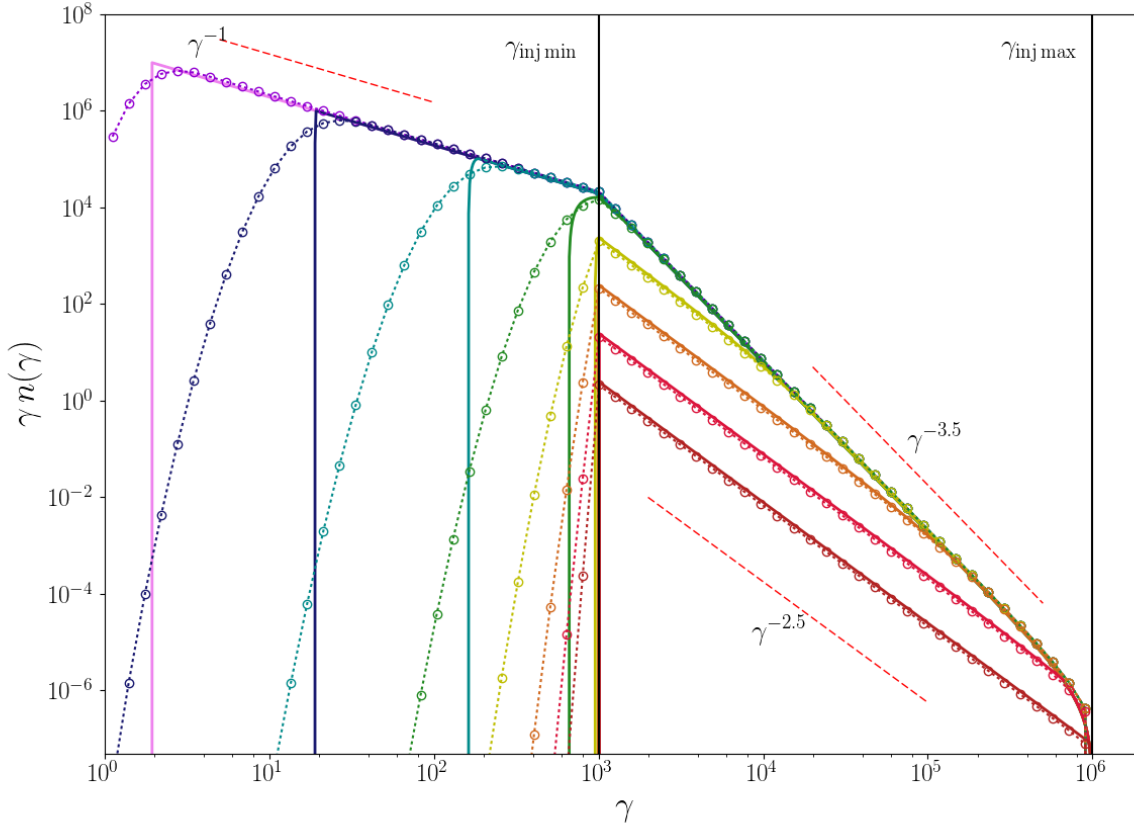


Figure 3. Results of a test with constant particle injection with slope $p = 3.5$ between $\gamma_{\text{inj,min}} = 50$ and $\gamma_{\text{inj,max}} = 5 \times 10^5$ coupled with synchrotron cooling in a uniform magnetic field with $B = 200$ G. The injection distribution is normalized so that the total injection rate is $1000 \text{ particles cm}^{-3} \text{ s}^{-1}$. The numerical solution from KORAL’s implicit solver (open circles) is compared with the analytic solution (solid lines) at times $t = 10^{-3}, 10^{-2}, 10^{-1}, 1, 10, 10^2, 10^3$ and 10^4 seconds. The spectrum develops a cooling break between the injection slope p for $\gamma < \gamma_{\text{brk}}$ and $p + 1$ for $\gamma > \gamma_{\text{brk}}$. The cooling break starts at large γ and propagates toward lower γ until the spectrum is broken over the entire injection range at $t = 10$ s. After this time, the spectrum cools to $\gamma < \gamma_{\text{inj,min}}$ with slope $p = 2$. The sharp discontinuity at the lower end of $n(\gamma)$ is smeared out in the numerical KORAL solution because of diffusion in the upwind finite differencing method we use. However, KORAL accurately captures the location of the peak of $\gamma n(\gamma)$ as it propagates to lower energies.

4.3 Synchrotron and Inverse Compton Cooling

We check the implementation of radiative cooling in KORAL’s implicit solver with two tests in a flat, zero-velocity gas background with constant injection of nonthermal electrons.

In the first test, we inject particles with a power-law slope $p = 3.5$ between $\gamma_{\text{inj,min}} = 50$ and $\gamma_{\text{inj,max}} = 5 \times 10^5$ and subject them to synchrotron cooling in a constant magnetic field of $B = 200$ G. Under constant injection and synchrotron cooling, and for $t < t_{\text{syn}}$, the particle spectrum develops a cooling break from the injection power-law slope $-p$ to a slope $-(p + 1)$ at γ_{brk} given by

$$\begin{aligned} \gamma_{\text{brk}} &= (1/\gamma_{\text{inj,max}} - b_s t)^{-1}, \\ b_s &= 1.292 \times 10^{-9} (B/1 \text{ G})^2, \end{aligned} \quad (50)$$

where the time t_{syn} is

$$t_{\text{syn}} = (\gamma_{\text{inj,min}}^{-1} - \gamma_{\text{inj,max}}^{-1})/b_s. \quad (51)$$

At $t = t_{\text{syn}}$, the cooling break reaches $\gamma_{\text{inj,min}}$, and at later

times the spectrum cools to $\gamma < \gamma_{\text{inj,min}}$ with a power-law slope of -2 .

The results from KORAL are compared with the analytic solution in Fig. 3. The development of the synchrotron cooling break and its propagation to lower particle energies with time is clearly captured in the KORAL solution. At the low resolutions we use, the numerical solution from KORAL cannot capture the sharp cutoff at low particle energies, and produces a tail extending to low γ (note that the vertical scale is over 14 orders of magnitude, so the discrepancy is not serious). However, the location of the peak in the spectrum as a function of time is reproduced well.

As another test of the KORAL implicit solver for radiative nonthermal cooling, we replicate a problem from Manolakou et al. (2007), which demonstrates the effects of the Klein-Nishina cross section in the inverse Compton cooling term (equations. 33 and 35). Neglecting bremsstrahlung radiation

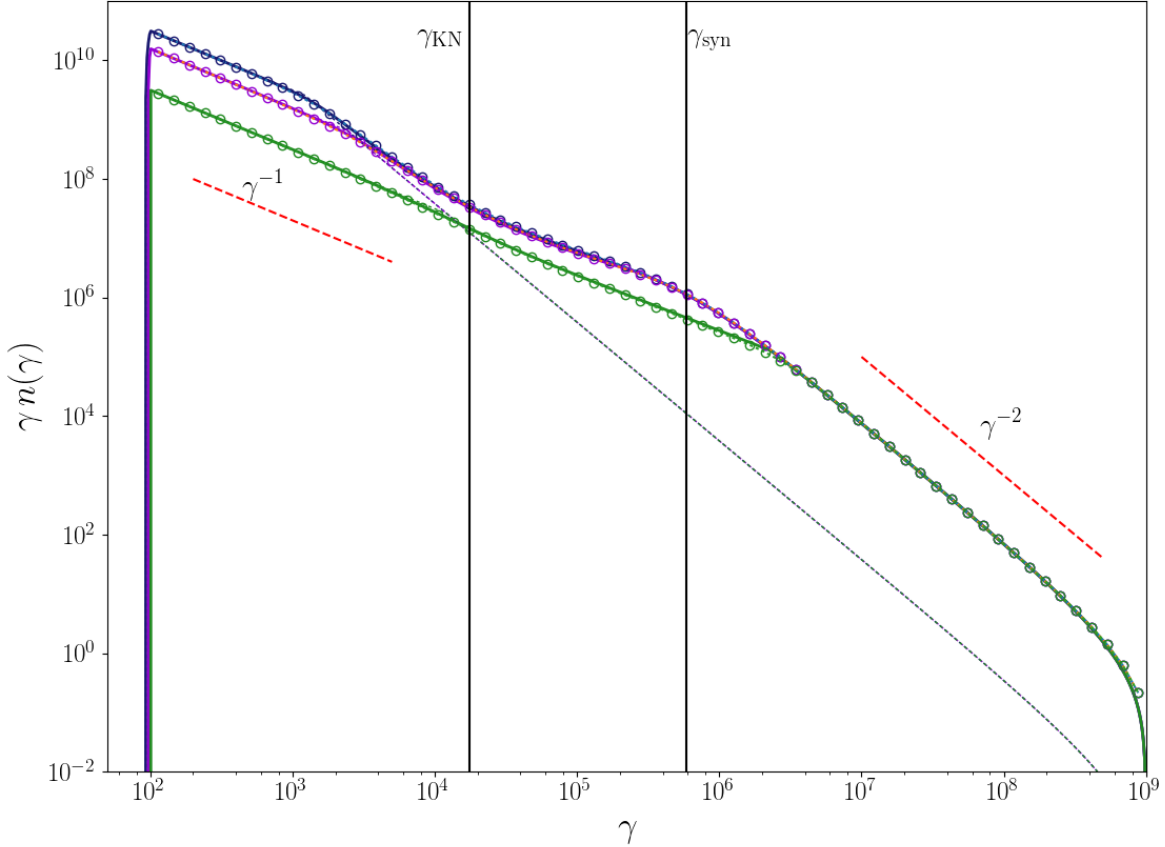


Figure 4. Nonthermal energy distribution evolution in an environment with $B = 10 \mu\text{G}$, $u_{\text{rad}} = 8.01 \times 10^{-10} \text{ erg cm}^{-3}$, and $T_{\text{rad}} = 30000 \text{ K}$. We inject particles in a power law with $p = 2$ between $\gamma_{\text{inj,min}} = 100$ and $\gamma_{\text{inj,max}} = 10^9$. The numerical solution from KORAL’s implicit solver (open circles) is compared with the semi-analytic solution (solid lines) at times $t = 10^5$ (green), 5×10^5 (purple) and 10^6 yr (blue). Note the excellent agreement. The analytic solution for the same problem neglecting the Klein-Nishina cross section of electrons (taking $F_{KN} = 1$ in equation 33) is also displayed (dotted lines).

and Coulomb coupling, the cooling rate is

$$\dot{\gamma} = b_{\text{syn}} \gamma^2 \left[1 + \frac{u_{\text{rad}}}{u_{\text{mag}}} (1 + 4\gamma\epsilon_0)^{-3/2} \right], \quad (52)$$

where $b_{\text{syn}} = -1.292 \times 10^{-11} (B/1 \text{ G})^2$ and $\epsilon_0 = kT_r/m_e c^2$. We set up a test in a uniform background similar to a stellar environment dominated by hot young stars (Manolakou et al. 2007). We set $B = 10 \mu\text{G}$ and assume a photon bath with energy density $u_{\text{rad}} = 7.95 \times 10^{-10} \text{ erg cm}^{-3}$ and temperature $T_{\text{rad}} = 30000 \text{ K}$. We inject particles in a power law with $p = 2$ between $\gamma_{\text{inj,min}} = 100$ and $\gamma_{\text{inj,max}} = 10^9$, normalized so that the total injection rate is $10^{-3} \text{ particles cm}^{-3} \text{ s}^{-1}$.

We compute the spectrum as a function of time using the semi-analytic method of Manolakou et al. (2007). The results are displayed in Fig. 4 at times $t = 10^5$, 5×10^5 , and 10^6 yr . The KORAL solution (open circles) lines up well with the semi-analytic solution (solid lines), demonstrating the code’s ability to accurately capture details of the ra-

diative cooling of nonthermal distributions beyond simple synchrotron cooling.

The solution in this test displays different behavior in three distinct regimes. From equation (52), at the highest energies, $\gamma > \gamma_{\text{syn}} = ((u_{\text{rad}}/u_{\text{mag}})^{2/3} - 1)/4\epsilon_0$, the solution is dominated by synchrotron cooling. Hence the spectrum shows a characteristic synchrotron cooling break above γ_{syn} , where the slope becomes $-(p+1) = -3$. Equation (52) also indicates that below $\gamma_{KN} \approx 1/4\epsilon_0$, the Thomson limit applies. Between γ_{KN} and γ_{syn} , the decrease in the cooling rate due to the Klein-Nishina cross section causes the spectrum to harden compared to what is predicted when only Thomson scattering is considered (dotted lines in Fig. 4). As time progresses, electrons initially injected at $\gamma_{\text{inj,max}}$ cool to lower energies γ_{cool} . By the last time shown, $\gamma_{\text{cool}} < \gamma_{KN}$; electrons injected at the highest energies have cooled below the energies where the Klein-Nishina cross section dominates, and Thomson cooling begins to break the spectrum for $\gamma < \gamma_{KN}$.

Because the cooling rates in this problem are so low,

even over 10^6 years the spectrum does not have time to cool much below the injection range. Therefore, the implicit solver does not have to deal with abrupt discontinuities in the spectrum, and except for the slight smoothing out of the synchrotron break, the obvious diffusion seen in the tests in Figs. 2 and 3 is not apparent here.

5 TEST SIMULATION OF SGR A*

As a test of the entire code with all elements included, we have carried out 2D simulations of an accreting black hole with parameters appropriate for the accretion flow in Sgr A*. We have run both a pure thermal model with a two-temperature plasma (two fluid populations, thermal ions and thermal electrons, similar to Sądowski et al. 2017), and a nonthermal model with all three fluid populations (thermal ions, thermal electrons and nonthermal electrons, §2.1).

For the injection properties of the nonthermal population we use a very simple ad hoc prescription, which is sufficient for the current test, but will need to be improved in the future for modeling real systems. We assume that a constant fraction of the local viscous electron heating rate goes into nonthermal electrons, with a fixed energy spectrum that is independent of location in the simulation box. However, the observed infrared and X-ray variability of Sgr A* (Dodds-Eden et al. 2011; Neilsen et al. 2013) suggests that the nonthermal acceleration mechanism is localized, either in magnetic reconnection regions (Sironi & Spitkovsky 2014) or in shocks (Guo et al. 2014). Recently, Ball et al. (2016) showed that the X-ray variability of Sgr A* could be qualitatively reproduced by adding a nonthermal distribution by hand in regions of high magnetization in a single-fluid GRMHD simulation. In a future work, we will consider full GRMHD+nonthermal electron simulations using more elaborate injection prescriptions informed by these studies.

5.1 Units

We work in a Schwarzschild spacetime (non-spinning black hole) with black hole mass $M = 4 \times 10^6 M_\odot$, the estimated mass of Sgr A* (Gillessen et al. 2009; Chatzopoulos et al. 2015). We use the gravitational radius $r_g = GM/c^2 = 6 \times 10^{11}$ cm = 0.04 AU as our unit of length, and $t_g = r_g/c = 20$ s as our unit of time. We define the Eddington accretion rate as

$$\dot{M}_{\text{Edd}} = \frac{L_{\text{Edd}}}{\eta c^2} = \frac{4\pi GMm_p}{\eta c \sigma_T}, \quad (53)$$

where L_{Edd} is the Eddington luminosity, and we use an efficiency $\eta = 0.057$ appropriate for a non-spinning black hole. For the $4 \times 10^6 M_\odot$ black hole we consider, the Eddington accretion rate $\dot{M}_{\text{Edd}} = 0.16 M_\odot \text{ yr}^{-1}$, and the Eddington luminosity $L_{\text{Edd}} = 5 \times 10^{44} \text{ erg s}^{-1}$.

5.2 Model Setup

The simulations are performed in Kerr-Schild coordinates using an axisymmetric 2D grid with a resolution of 256×256 cells in radius and polar angle. The radial cells are distributed exponentially from inside the BH horizon at $1.85 r_g$ to $1000 r_g$, and the polar angle cells are uniformly sampled.

The initial fluid conditions are identical to the model Rad8SMBH in Sądowski et al. (2017). We initialize the simulation with a hydrostatic equilibrium torus with parameters as in Narayan et al. (2012). The torus has an inner edge at $10 r_g$ and is threaded by a weak magnetic field. The initial electron and ion temperatures are set equal to the initial gas temperature, and there are no nonthermal electrons. The torus is surrounded by a static atmosphere with negligible mass and radiation energy density, but with the radiation temperature everywhere set to 10^5 K.

We ran the model for a total time of $2 \times 10^4 t_g$ with non-thermal electron evolution turned off. The thermal electron and ion populations were heated using the viscous heating prescription of Howes (2010). They exchanged energy with each other via thermal Coulomb coupling, and the thermal electrons radiated via synchrotron, bremsstrahlung, and inverse Compton scattering. We used the mean-field dynamo from Sądowski et al. (2015) to prevent the decay of the axisymmetric magnetic field. We refer to this purely thermal simulation as the *control run*.

In the control run, gas begins accreting on the black hole around $t \sim 3000 t_g$, and by $t = 10^4 t_g$, the accretion is in steady state and we can estimate the mass accretion rate on the black hole. At this time, we scale the gas density, and correspondingly the magnetic field strength, to achieve the desired accretion rate of $\approx 4 \times 10^{-8} \dot{M}_{\text{Edd}}$ appropriate for Sgr A*. We run the model with the rescaled density from $t = 10^4 t_g$ up to $2 \times 10^4 t_g$. We use the data from the time period $1.5 \times 10^4 - 2 \times 10^4 t_g$ to study the properties of the accretion flow.

Having run the control model described above, we then simulate a system with nonthermal electrons included. We refer to this simulation as the *nonthermal run*. We start this simulation with the output from the control run at time $10^4 t_g$, and rescale the density and magnetic field as before. However, we now include nonthermal electron injection, and we evolve the system from $t = 10^4 t_g$ up to $2 \times 10^4 t_g$ with all the nonthermal interactions turned on. We track the non-thermal electron energy distribution over $N = 32$ bins ranging from $\gamma_{\text{min}} = 200$ to $\gamma_{\text{max}} = 2 \times 10^6$. We chose γ_{min} to be above the characteristic electron energy $\theta = k_B T / m_e c^2$ for a temperature at the high end of the range observed in the control model, around $T \sim 10^{12}$ K. We then chose γ_{max} so as to cover four decades of γ in the nonthermal distribution. With a resolution of 8 points per decade, this corresponds to a total of $N = 32$ nonthermal electron bins.

For the nonthermal injection, we fix the power-law index at $p = 3.5$, consistent with past studies (Özel et al. 2000; Yuan et al. 2003) and with observational constraints (Porquet et al. 2008; Barrière et al. 2014). We inject the electrons between $\gamma_{\text{inj min}} = 500$ and $\gamma_{\text{inj max}} = \gamma_{\text{max}} = 2 \times 10^6$. We offset the minimum injected γ from the lowest Lorentz factor γ_{min} tracked by the code in order to prevent the immediate cooling of electrons injected at γ_{min} back into the thermal population (equation 39). We set the nonthermal heating fraction to $\delta_{\text{nth}} = 0.015$ (Özel et al. 2000; Yuan et al. 2003; Ball et al. 2016; Mao et al. 2016). The total electron heating fraction δ_e , of which 98.5 per cent goes to the thermal species, is determined using the prescription of Howes (2010), which is a (strong) function of the magnetization parameter $\beta = p_{\text{gas}}/p_{\text{mag}}$.

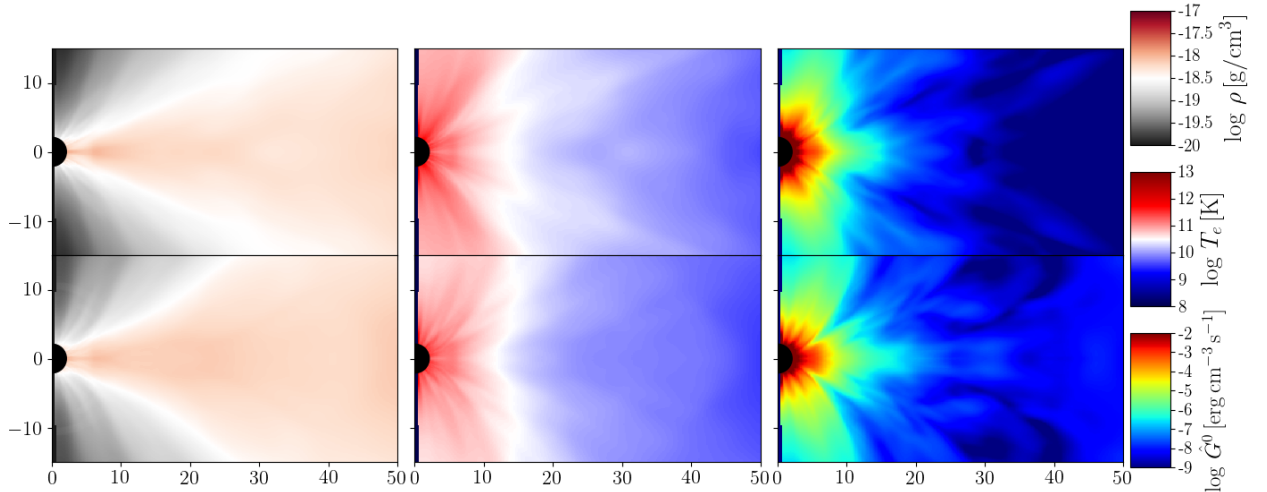


Figure 5. Comparison of time-averaged quantities in the control thermal run (top row) and the nonthermal run (bottom row). Averages are taken over the period $t = 1.5 \times 10^4 - 2 \times 10^4 t_g$, and the distributions are symmetrized about the equatorial plane. In each column, the same color scale is used in the upper and lower panels. From left to right, the quantities shown are the gas density ρ , the electron temperature T_e , and the fluid frame radiation power $-\hat{G}^0$. The presence of nonthermal electrons does not significantly affect either ρ or T_e . However, the nonthermal model has significantly more radiative power, especially at larger radii.

5.3 Comparison of Thermal and Nonthermal Models

In Fig. 5, we compare time-averaged spatial distributions of several quantities in the control (thermal) run with those in the nonthermal run. For each model, we average the quantities over the time range $t = 1.5 \times 10^4 - 2 \times 10^4 t_g$, and also symmetrize around the equatorial plane for additional smoothing of the results. Shown are the density ρ , electron temperature T_e , and the fluid frame radiation power $-\hat{G}^0$ computed from average primitives.

Fig. 5 indicates that the overall structure and distribution of the gas density and electron temperature are similar in the two models. This is expected, since the fraction of electron energy that goes into the nonthermal electrons is only 1.5 per cent. Furthermore, the accretion flow in our model is optically thin and radiatively inefficient, so the emission from the nonthermal electrons does not significantly alter the gas dynamics. Indeed, the gas dynamics and electron and ion thermodynamics in both the control run and the nonthermal run are quite similar to model Rad8SMBH in Sądowski et al. (2017).

The last column of Fig. 5, however, shows that the rest frame power of the emitted radiation is not the same in the control and nonthermal runs — it is enhanced in the latter run, most significantly at large radii. The spatial distribution of the nonthermal emission is purely the result of the particular injection prescription we use. We inject nonthermal electrons with the same energy fraction $\delta_{\text{nth}} = 0.015$, in the same power-law distribution, everywhere in the simulation. In addition, the magnetic field strength is fairly constant ($B \sim 10$ G) over most of the region of interest. Therefore, the amount of nonthermal synchrotron emission is directly proportional to the viscous heating rate of the gas. On the other hand, the thermal electron temperature varies substantially with radius, falling to below $\sim 10^{10}$ K by a radius of $30 r_g$. Since thermal synchrotron power varies as T_e^2 , the

thermal emission falls rapidly with increasing radius. Thus, the thermal electrons are more advection-dominated at large radii compared to the nonthermal electrons.

5.4 Nonthermal Simulation

Figs. 6 and 7 show time-averages and snapshots of several quantities in the nonthermal run. The snapshot in these comparisons (right side of each panel) corresponds to $t = 1.8 \times 10^5 t_g$ and the time-averaging (left side of each panel) is done from $t = 1.5 \times 10^4 - 2 \times 10^4 t_g$.

The top panel in Fig. 6 shows the gas density ρ . As expected, and as seen also in the control run (Fig. 5), the disc is geometrically thick and turbulent, the latter evident in the snapshot density distribution (even more so in the temperature distribution discussed next). The blue contour corresponds to the location where the accretion time-scale t_{acc} in the time-averaged model is equal to the time-averaging duration $5000 t_g$. The accretion time scale is defined as

$$t_{\text{acc}} \equiv \frac{r}{\sqrt{v_r^2 + r^2 v_\theta^2}}. \quad (54)$$

Since the total duration of the nonthermal run is $10^4 t_g$, the above limit is a conservative estimate of the region of inflow equilibrium (it corresponds to the ‘strict’ criterion, as defined in Narayan et al. 2012). We can be confident that any region of the flow that lies inside the surface defined by the above limit has reached steady state and has forgotten the initial conditions when relativistic electron injection was first turned on.

The second panel in Fig. 6 shows the electron temperature, which ranges from $\sim 10^{10}$ K in the disc at $r \approx 30 r_g$ to 10^{12} K in the funnel region. In very low accretion rate systems such as Sgr A*, both radiative cooling and Coulomb coupling are weak and neither is capable of controlling the electron temperature (Yuan & Narayan 2014). The temperature is thus primarily determined by the viscous heating

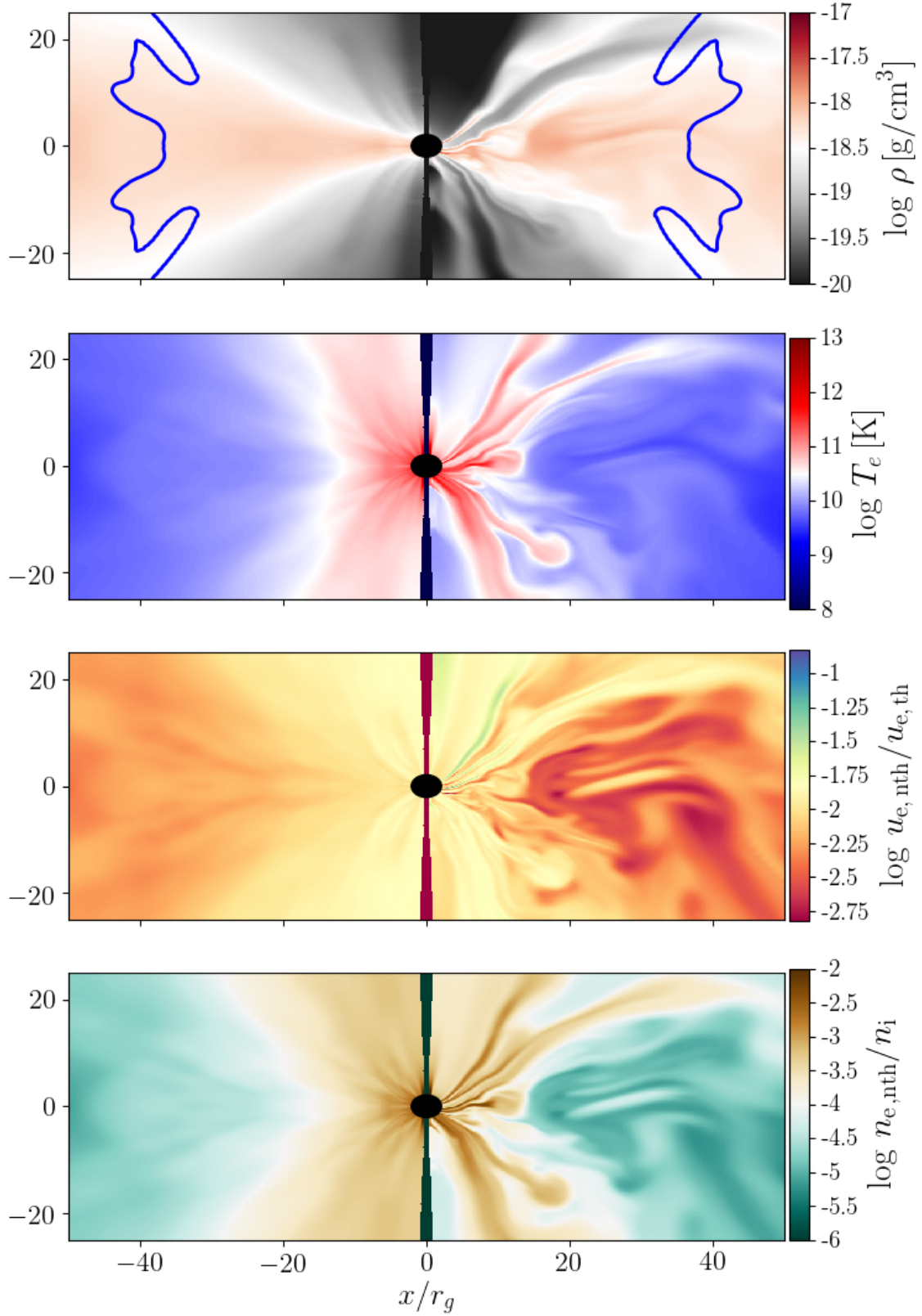


Figure 6. Snapshot (right) and time-averaged (left) distributions of (from top to bottom) gas density ρ , thermal electron temperature T_e , ratio of nonthermal to thermal electron energy densities $u_{e, \text{nth}}/u_{e, \text{th}}$, and fraction of electrons in the nonthermal distribution $n_{e, \text{th}}/n_i$. The blue contour in the first panel encloses the region of the simulation that is in inflow equilibrium, as determined by equation (54).

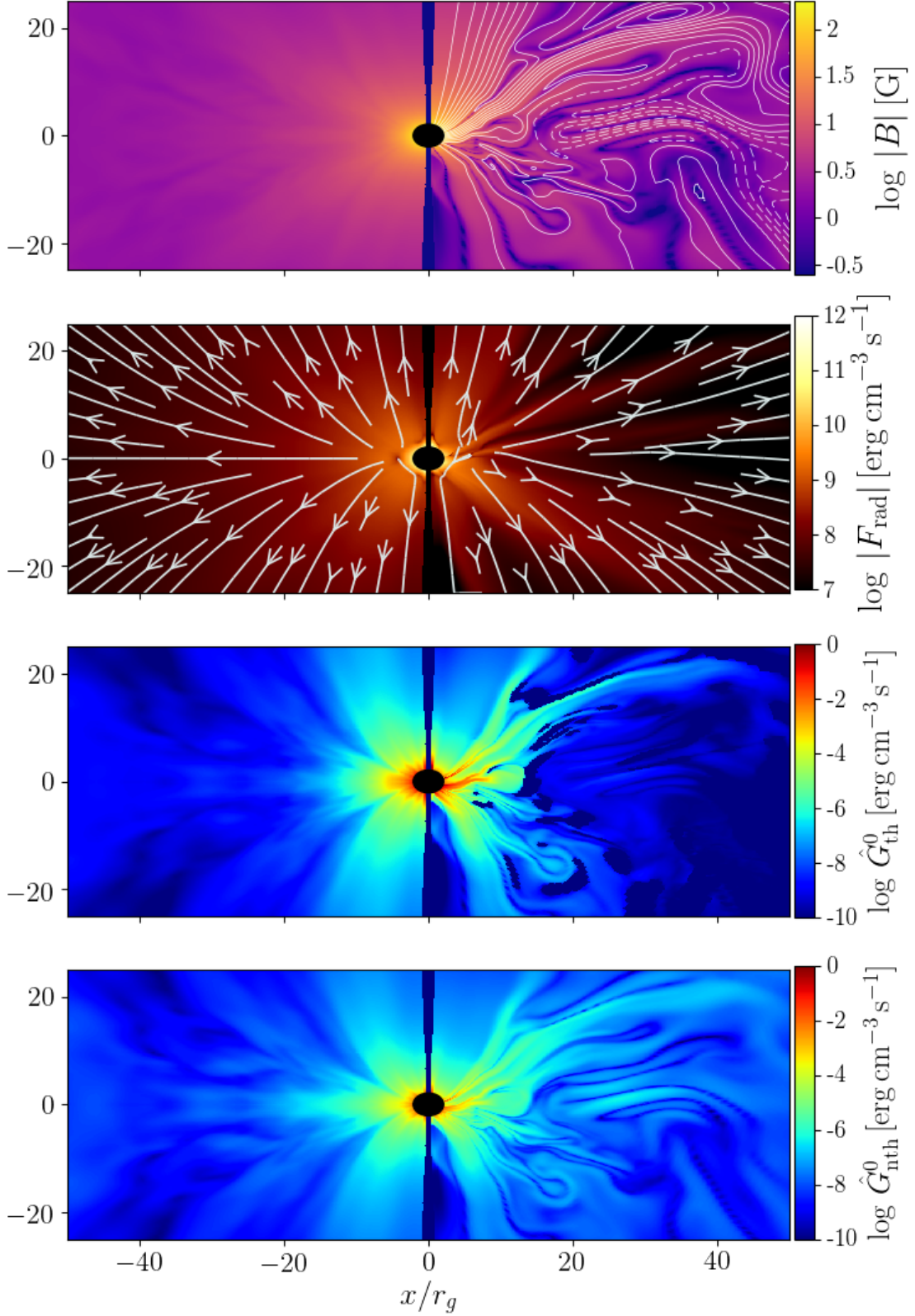


Figure 7. Snapshot (right) and time-averaged (left) distributions of (from top to bottom) magnetic field strength $|B|$, magnitude of the radiation flux $|F|$, fluid frame radiation power from thermal electrons $-\hat{G}_{\text{th}}^0$, and fluid frame radiation power from nonthermal electrons $-\hat{G}_{\text{nth}}^0$. Contours in the first panel show poloidal magnetic field lines. Streamlines in the second panel show the direction of the radiation flux.

and is highly dependent on the heating fraction δ_e . Our prescription (Howes 2010) has high $\delta_e \approx 1$ in regions of high magnetization, which explains the high temperature in the polar region (where $\beta < 1$) compared to the equatorial plane (where typically $\beta > 5$).

The third panel in Fig. 6 shows the ratio of the energies in nonthermal and thermal electrons. Since the radiative and Coulomb coupling between the two species is weak, the energy ratio should be set primarily by the injection ratio δ_{nth} , which we have fixed at 1.5 per cent throughout. In much of the equatorial plane out to $r \approx 30 r_g$, the energy ratio is indeed approximately equal to δ_{nth} . Regions where the ratio is lower than δ_{nth} correspond to places where the electron temperature is lowest. In these regions, the overall electron heating fraction δ_e is small and there has not been enough injection of nonthermal particles to bring the energy up to the injection value. Conversely, in the snapshot distribution, we see some regions where the nonthermal-to-thermal energy ratio exceeds δ_{nth} . In these regions, the thermal electrons are heated to high temperatures $\sim 10^{12}$ K. At these temperatures, the thermal electrons that produce most of the synchrotron emission have Lorentz factors $\gamma > 500$, greater than the minimum $\gamma_{\text{inj min}}$ of the injected nonthermal electrons. These high- γ thermal electrons lose energy rapidly to radiation, lowering their energy relatively more quickly compared to the nonthermal electrons.

Finally, the fourth panel in Fig. 6 shows the overall fraction of the electron population that is in the nonthermal distribution. In the snapshot image, regions with a high ratio of nonthermal electrons to the total population are coincident with regions of high thermal electron temperature (second panel). This is because both distributions are primarily driven by the fraction δ_e of electron viscous heating (since δ_{nth} is fixed).

In Fig. 7, we display quantities related to the cooling and radiation from nonthermal particles. The top panel shows the magnetic field strength, which is on average ~ 10 G throughout much of the region in inflow equilibrium ($r \lesssim 40 r_g$). However, the snapshot on the right shows considerable evidence for turbulence and deviations from the mean. Regions with a stronger magnetic field in the snapshot image correlate with regions of higher thermal electron temperature (second panel of Fig. 6); this is expected since the electron energy injection fraction δ_e increases with magnetization. In addition, since the nonthermal injection rate is proportional to δ_e , the same regions also stand out in the snapshot distribution in the fourth panel of Fig. 6.

The second panel in Fig. 7 shows the magnitude of the radiation flux \tilde{F}^i , represented by the color scale, with streamlines indicating the direction of the flux vector. Since the accretion flow is highly optically thin, radiation is emitted more-or-less isotropically and freely streams out of the system.

The third and fourth panels in Fig. 7 show the fluid frame power in radiation from thermal and nonthermal electrons, respectively. The thermal emission dominates in the inner regions up to $r \sim 10 r_g$, and then declines rapidly at larger radii where the electrons are cooler. However, as previously discussed, highly energetic nonthermal electrons are present even at large radii, because of our simple injection prescription. Therefore, there is significant nonthermal synchrotron emission out to $r \sim 50 r_g$. The two snapshot panels

show that the instantaneous radiation power in both thermal and nonthermal emission traces the regions of strongest magnetic field in the top panel.

5.5 Synchrotron Break

The dominant physical processes shaping the evolution of the nonthermal electron energy distribution $n(\gamma)$ in the nonthermal simulation are electron injection and synchrotron cooling. As the nonthermal particles cool via synchrotron emission, the spectrum will break from the injection power-law slope $-p = -3.5$ to $-(p+1) = -4.5$. The γ_{brk} at which the break occurs moves to lower values with increasing time. From equation (51), under constant injection and given a characteristic magnetic field strength of $B \sim 10$ G, γ_{brk} will move all the way down to $\gamma_{\text{inj min}}$ in 1.5×10^4 s, or $780 t_g$. However, in the actual simulation, non-constant particle injection rates, adiabatic compression, and advection modify the development of the synchrotron break and can shift the break Lorentz factor to higher γ , with advection having the strongest effect.

In the top panel of Fig. 8, we plot the ratio of the synchrotron cooling time (equation 51) to the accretion/advection time-scale (equation 54). We find that this ratio is > 1 almost everywhere in the region considered, which indicates that, before the spectrum can break fully, the gas is advected away or falls into the black hole.

The second panel of Fig. 8 shows the Lorentz factor γ_{brk} of the synchrotron cooling break in the nonthermal distribution. We determine γ_{brk} in each cell simply by finding the maximum of $\gamma^{p+1/2}n(\gamma)$. By the late times we are considering, the cooling break has propagated to low Lorentz factors, but since the accretion time-scale is shorter than the cooling time-scale, the break still lies above $\gamma_{\text{inj min}}$. In much of the disc, the break is around $\gamma_{\text{brk}} \sim 3000$. In the funnel region, gas moves with high velocities either into the BH or out along the axis; the corresponding small inflow/outflow (advection) time-scale means that electrons do not have enough time to cool before being swept away. Thus, the break Lorentz factors in the funnel are typically higher than in the rest of the simulation, $\gamma_{\text{brk}} \sim 10^4$.

In the time-averaged distribution, the ratio of synchrotron to advection times can provide a quick estimate of the break Lorentz factor. In the funnel regions, where $t_{\text{syn}}/t_{\text{acc}} \approx 100$, we can estimate the position of the break by substituting $t_{\text{syn}}/100$ in equation (50); the result is $\gamma_{\text{brk}} \approx 5 \times 10^4$. A comparison with the second panel shows that this quick estimate is reasonably good.

The snapshot distribution of break Lorentz factor shows more structure than the average. Much of this structure is due to the turbulent magnetic field, which creates regions of short and long synchrotron cooling times. However, the regions with high γ_{brk} do not always have a one-to-one correspondence with regions of large $t_{\text{syn}}/t_{\text{acc}}$ (see e.g. around $x = 20 r_g$, $z = 10 r_g$). This is because, in addition to synchrotron cooling and advection, other processes – particularly adiabatic compression – can shape the spectrum. Compression acts to push the entire distribution to higher γ , so it naturally pushes the break Lorentz factor to a higher γ than predicted by equation (50). In future studies, we will examine the effects of adiabatic compression on the spectrum in more detail.

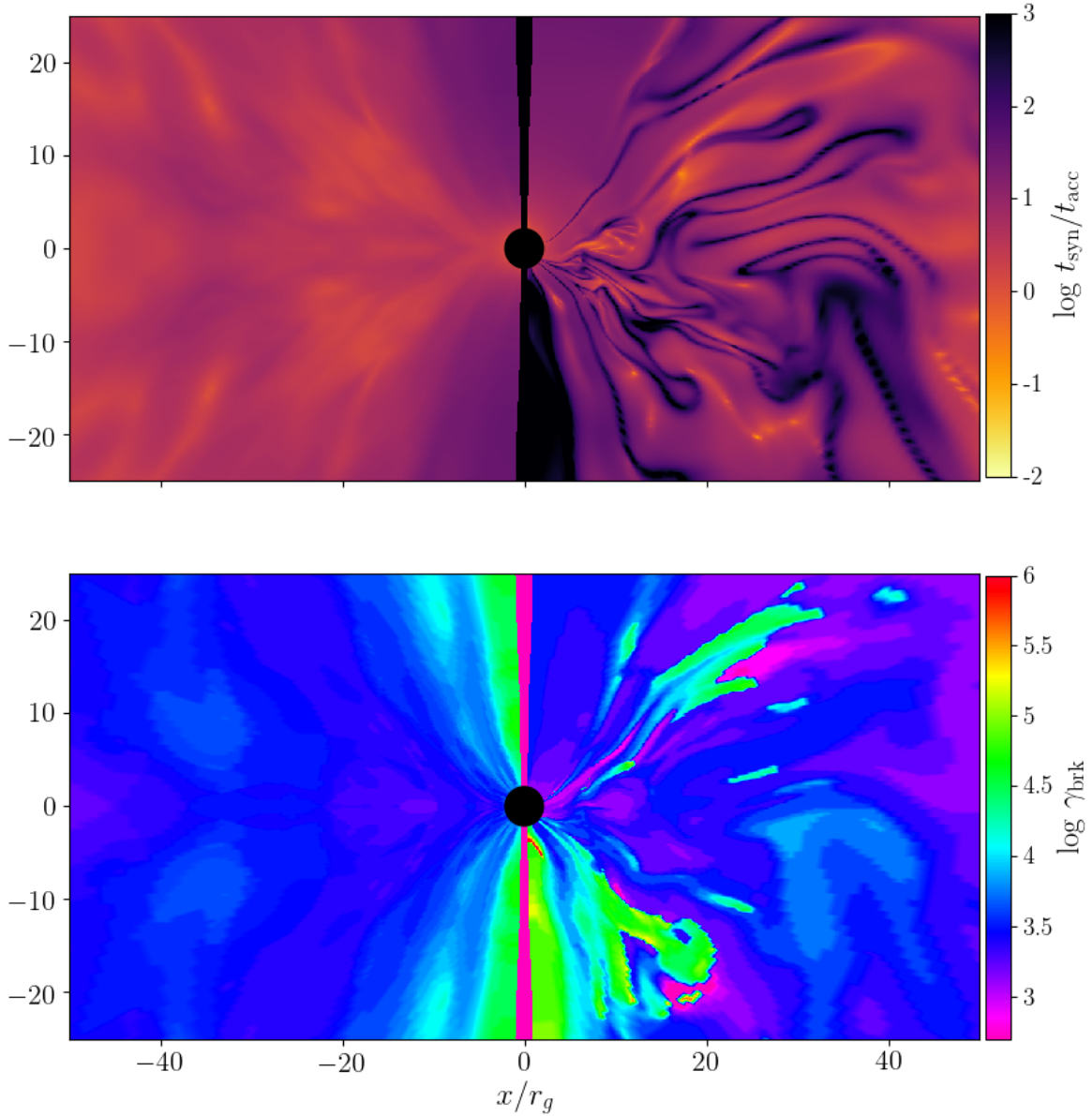


Figure 8. (Top) Ratio of synchrotron cooling time-scale to accretion time-scale, $t_{\text{syn}}/t_{\text{acc}}$, for a snapshot at $t = 1.8 \times 10^4 t_g$ (right) and corresponding ratio computed from time-averaged primitives (left). (Bottom) Location of the synchrotron cooling break Lorentz factor γ_{brk} . The cooling break is at higher γ in regions where $t_{\text{syn}}/t_{\text{acc}}$ is large. Electrons in such regions are advected away before they can be cooled by the magnetic field.

5.6 Spectra and Images

We computed spectral energy distributions (SEDs) for both the thermal-only control model and the full nonthermal model using `grtrans`,⁴ an open-source (polarized) ray tracing and radiative transfer code for black hole spacetimes (Dexter 2016). We modified `grtrans` to compute the non-thermal synchrotron emissivity j_ν and absorption coefficient α_ν directly from the local magnetic field and the appropriate integrals over the nonthermal electron energy distribution $n(\gamma)$ (Rybicki & Lightman 1986, equations 6.33

and 6.50;⁵ for recent work on integrating polarimetric synchrotron emissivities for various electron distribution functions see Leung et al. 2011 and Pandya et al. 2016). The integrals for j_ν and α_ν are

$$j_\nu = \frac{\sqrt{3}}{4\pi^2} \frac{e^3 B \sin \alpha}{mc^2} \int n(\gamma) F\left(\frac{\nu}{\nu_c}\right) d\gamma, \quad (55)$$

$$\alpha_\nu = \frac{4\pi}{3\sqrt{3}} \frac{e}{B \sin \alpha} \int \frac{n(\gamma)}{\gamma^5} K_{5/3}\left(\frac{\nu}{\nu_c}\right) d\gamma. \quad (56)$$

⁵ Note that to derive equation (56) from Rybicki & Lightman (1986) equation 6.50, we perform an integration by parts and discard the boundary term.

⁴ <https://github.com/jadexter/grtrans>

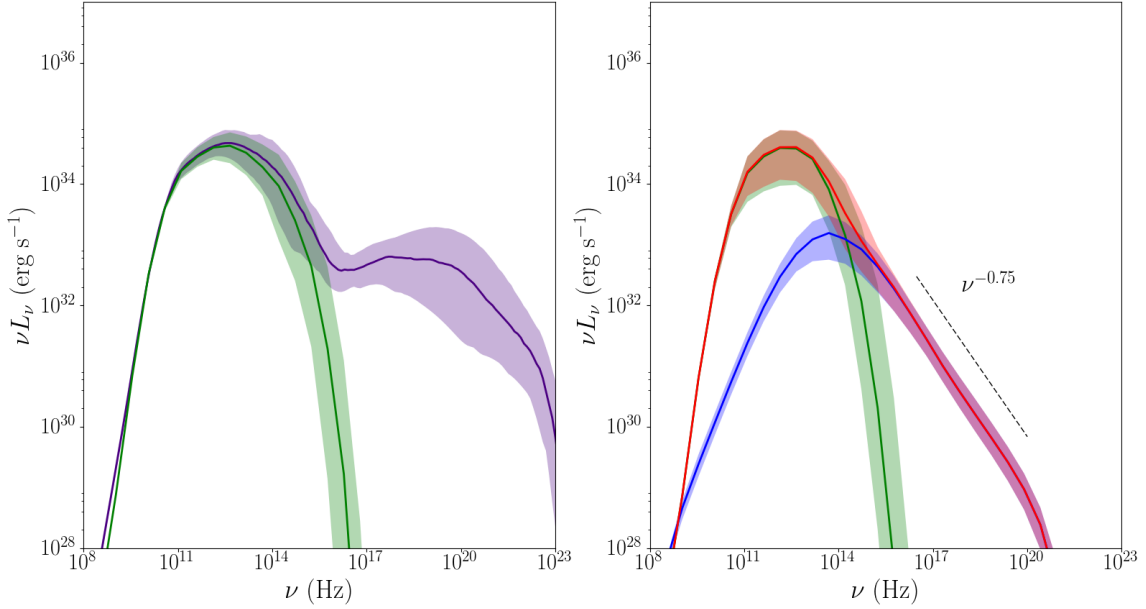


Figure 9. (Left Panel) Median spectral energy distribution (solid lines) of the thermal control run computed from the snapshot data from 15,000-20,000 t_g , as observed at an angle of 60° with respect to the disc polar axis. The shaded regions represent the 68 per cent confidence interval (nominal 1σ range) for the time-variability of the spectra in this interval. The green spectrum is obtained using `grtrans` (Dexter 2016), which includes only synchrotron radiation. The indigo spectrum was computed with `HEROIC` (Narayan et al. 2016), including bremsstrahlung emission and inverse Compton scattering. (Right Panel) Synchrotron-only spectra of snapshots from the nonthermal simulation in the range 15,000-20,000 t_g computed with `grtrans`. The green and blue lines show the spectra of the thermal and nonthermal electrons, respectively, and the red line shows the total spectrum of both populations combined. The dashed line shows the expected power-law slope produced by the broken spectrum of nonthermal electrons, $L_\nu \propto \nu^{-p/2} \propto \nu^{-1.75}$.

In the above expression, α is the pitch angle between the line of sight and the magnetic field in the fluid frame, $F(x) = x \int_x^\infty K_{5/3}(y) dy$ is the synchrotron function, and ν_c is the characteristic synchrotron frequency,

$$\nu_c = \frac{3eB\gamma^2 \sin \alpha}{4\pi m_e c}. \quad (57)$$

We performed the radiative transfer only for the total intensity (we plan to include polarization in the future). To speed up the computations, we used fitting functions for the synchrotron function $F(x)$ and Bessel function $K_{5/3}(x)$ from Fouka & Ouichaoui (2013).

The green curve in the left panel in Fig. 9 shows the median `grtrans` synchrotron SED from the thermal control run which was computed from the snapshot data from 15,000-20,000 t_g , as observed at an angle of 60° with respect to the disc polar axis. The shaded region represents the 68 per cent confidence interval (nominal 1σ range) for the time-variability of the spectrum in this interval. The spectrum peaks at $\nu \sim 10^{12}$ Hz, with a steep fall-off at lower frequencies because of self-absorption and a fall-off at higher frequencies because of the rapid decline in the number of thermal electrons at larger Lorentz factors.

The indigo curve in the same panel was computed using the post-processing code `HEROIC`, (Narayan et al. 2016; Zhu et al. 2015), which self-consistently solves for the spectrum and angular distribution of radiation at each position using the radiative transfer equation. The `HEROIC` radia-

tive transfer includes all radiation processes — synchrotron, bremsstrahlung, and inverse Compton scattering. In the synchrotron component, the `HEROIC` spectrum agrees very well with the `grtrans` spectrum except at frequencies below 10^{10} Hz. This small discrepancy arises because the `HEROIC` computations are done using simulation data out to a radius of $300 r_g$, whereas the `grtrans` calculations are limited to $50 r_g$, so `HEROIC` picks up more low-frequency emission from further out in the simulation volume. While the power in nonthermal radiation extends to larger radii than the thermal population (Fig. 5), nonthermal spectra from `grtrans` generated using data out to $100 r_g$ are nearly identical to the plots shown using a maximum radius of $50 r_g$.

The right panel in Fig. 9 shows spectra of the nonthermal run, computed with `grtrans` using the same parameters as the left panel. Similarly to the left panel, the solid lines are the median SEDs from the interval 15,000-20,000 t_g , and the shaded regions are the 68 per cent confidence range of the time variability. Since `HEROIC` does not presently include nonthermal electrons, we do not show comparison spectra from that code. Comparing the thermal-only (green curve) and the nonthermal-only (blue curve) `grtrans` spectra, we see that thermal emission dominates by far in the sub-millimeter band, nonthermal emission is modestly stronger at infrared wavelengths, and is the only contributor to the synchrotron emission at X-ray wavelengths. The power-law synchrotron emission is optically thin, and shows a characteristic slope $L_\nu \propto \nu^{1/3}$ at low frequencies. The

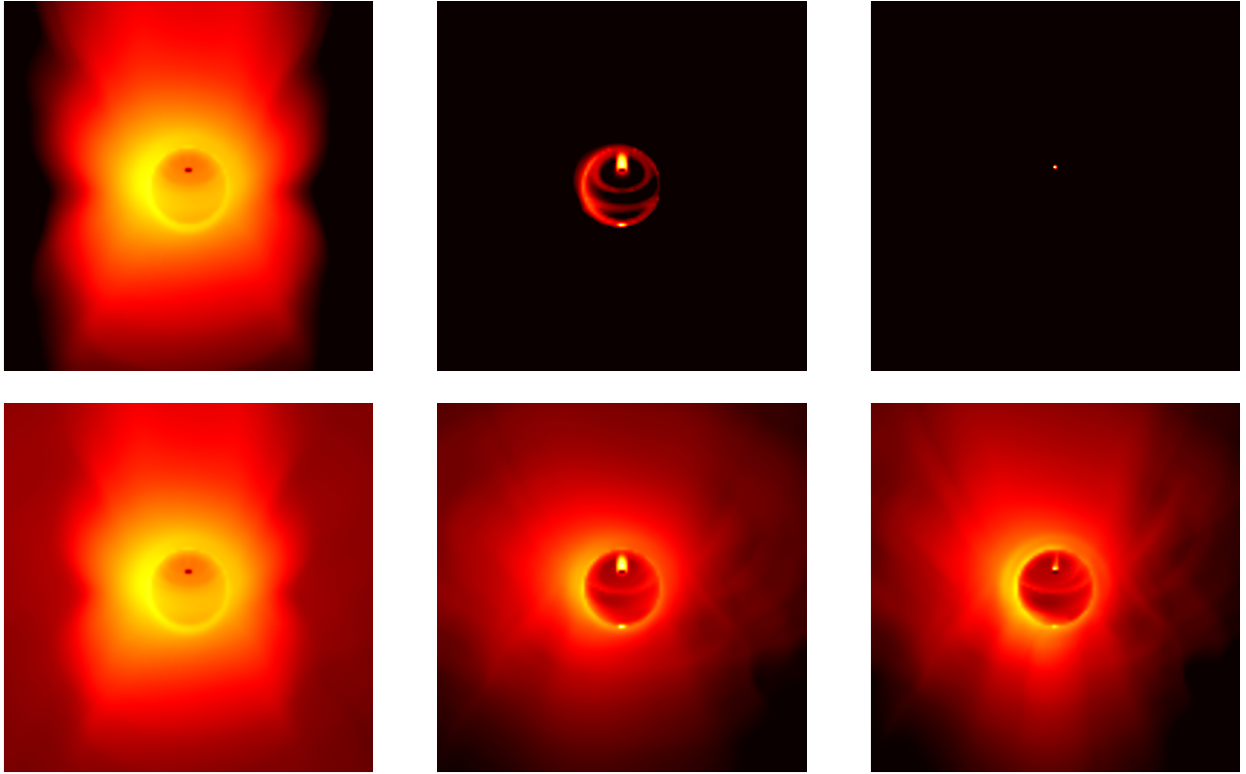


Figure 10. Images ($50 r_g$ wide, using logarithmic color maps) of synchrotron emission only, computed using `grtrans`, for the time-averaged control run (top row) and the nonthermal run (bottom row). The images correspond to 230 GHz sub-millimeter emission (left), 136 THz near-infrared emission (middle), and 2 keV X-ray emission (right).

power-law tail in the spectrum at high frequencies has a spectral slope $L_\nu \propto \nu^{-p/2} \propto \nu^{-1.75}$, as expected for a population of electrons with a distribution mostly broken to a power-law slope $-(p+1) = -4.5$.

The red curve in Fig. 9 shows the combined synchrotron emission from both thermal and nonthermal electrons. By and large, the combined spectrum is a direct sum of the two independent contributions, except at the lowest frequencies, where absorption by thermal electrons suppresses the nonthermal emission (Özel et al. 2000; Yuan et al. 2003). This effect is seen also in other recent studies in which synchrotron spectra from thermal and nonthermal electrons are computed by post-processing single temperature GRMHD simulations (Ball et al. 2016; Mao et al. 2016). Note that the spectra shown here include only thermal and nonthermal synchrotron emission. For more realistic nonthermal spectra, it will be necessary to incorporate synchrotron, bremsstrahlung, and inverse Compton scattering from nonthermal electrons into a global radiative transfer solver like HEROIC or a Monte Carlo transfer code such as `grmonty` (Dolence et al. 2009).

Sgr A* is known to be more variable in the infrared compared to sub-millimeter, and even more variable in X-rays (Eckart et al. 2006; Yusef-Zadeh et al. 2006; Dodds-Eden et al. 2009; Neilsen et al. 2013). From the variability in the spectra shown in the right panel of Fig. 9, it is clear that our uniform injection prescription generates little variability in the nonthermal synchrotron emission at high frequencies. However, the present simulations are not suitable for explor-

ing the variability in detail, both because they are in 2D — Sądowski & Narayan (2016) show that the variability properties of 2D and 3D simulations are different — and because we have used a toy prescription for nonthermal energy injection. The thermal spectrum in Fig. 9 shows that variability in the thermal X-ray inverse Compton spectrum exceeds that in the direct synchrotron emission at lower frequencies. Furthermore, a direct comparison of the thermal and nonthermal frequency-integrated inverse Compton power shows that while the thermal IC power dominates in the disc in the densest regions at small radii, the high energy of the nonthermal electrons (and the fact that the IC power grows as γ^2) leads to the nonthermal IC power exceeding the thermal IC power in the funnel region and in the disc at radii $\gtrsim 40 r_g$. Thus, we expect the nonthermal electrons to make a significant contribution to the high frequency spectrum and variability from IC emission. In sum, to accurately explore variability and flares from nonthermal electrons, we will need to extend our simulations to 3D, implement local injection prescriptions, and include bremsstrahlung and inverse Compton emission in the nonthermal radiative transfer. This is a promising direction for future work.

Fig. 10 shows `grtrans`-generated ray-traced images of the synchrotron emission from the time-averaged simulations at 3 frequencies: 230 GHz, which is near the thermal synchrotron peak and corresponds to the observing frequency of the Event Horizon Telescope (Doeleman et al. 2008), 136 THz in the near infrared, and 4.8×10^{17} Hz (2 keV) in X-rays. The images are 50 projected gravitational radii

across and displayed in a log scale. The bright regions of the image at 230 GHz are practically the same for the thermal and nonthermal runs, confirming that much of the emission is from thermal electrons. There is, however, additional extended flux at large radii in the bottom panel because of emission by nonthermal electrons. The ring in the infrared image is brighter when nonthermal electrons are included, and the emission extends to noticeably larger radii. The X-ray image is almost entirely from nonthermal emission. As for the spectra in Fig. 9, these results depend sensitively on the simple nonthermal energy injection prescription we have used. Bremsstrahlung emission and inverse Compton scattering will also modify these images, especially in X-rays

6 SUMMARY AND CONCLUSIONS

In this paper, we introduced a new algorithm to self-consistently evolve a population of nonthermal electrons in a black hole spacetime, in parallel with magnetized thermal gas and radiation. In each time step, a fraction of the viscously generated heat is used to heat some of the thermal electrons and to transfer them to the nonthermal population. The nonthermal electrons move with the fluid, and their energy distribution is modified by gas compression and expansion, Coulomb coupling, and radiative cooling. The back-reaction of the nonthermal electrons on the thermal population is automatically included.

We validated the algorithm on a variety of test problems, and presented first results on a 2D black hole accretion flow with nonthermal electrons. This simulation has a low mass accretion rate, roughly equal to the rate estimated in Sgr A*. As a result, the nonthermal distribution does not significantly affect the gas dynamics or thermodynamics of the thermal electrons or ions. However, the radiation power is enhanced, since the nonthermal electrons radiate more efficiently than their thermal counterparts. Furthermore, the energy distribution of the nonthermal electrons varies with location in the accretion flow. The distribution exhibits a synchrotron cooling break, and the break Lorentz factor γ_{brk} varies with position, being set by local conditions such as the magnetic field strength (which determines synchrotron power) and the gas velocity (which sets the effective advection time); γ_{brk} is also modified by other factors such as strong adiabatic compression.

The current work considers only one particularly simple prescription for injection into the nonthermal population. Specifically, we inject a fixed fraction of the local electron viscous heating into the nonthermal distribution, and we inject the nonthermal particles over a fixed range of γ , with a fixed power-law slope. The resulting simulation results are strongly influenced by these choices. A constant injection range of γ , independent of radius, ensures that nonthermal synchrotron emission dominates over thermal emission at large radii, where the temperature of the thermal electrons falls off rapidly. This is reflected in Fig. 10, which shows that at high frequencies, nonthermal electrons from farther out in the disc dominate the raytraced synchrotron image of the accreting gas. Furthermore, the choice of a minimum injection Lorentz factor $\gamma_{\text{inj},\text{min}} = 500$ means that most of the nonthermal emission is concentrated at infrared or higher frequencies, while the image at 230 GHz, of inter-

est for the Event Horizon Telescope, is basically unchanged compared to a purely thermal model. In principle, $\gamma_{\text{inj},\text{min}}$ should be chosen such that the nonthermal population connects smoothly to the thermal distribution, without a gap between the two. This will be necessary when we use the code to model real systems such as Sgr A*.

Another consequence of our choice of injection parameters is that the high frequency nonthermal emission in our simulation shows relatively little time variability. This is because nonthermal electrons are distributed relatively smoothly and uniformly throughout the simulation. The rapid variability that is observed in Sgr A* is likely driven by strong localized injection, perhaps from shocks or magnetic reconnection. This suggests a much more sporadic and localized injection of nonthermal energy, with small regions where the fraction of energy going into the nonthermal electrons, δ_{nth} , is much larger than the 1.5 per cent we chose in this work, and large regions elsewhere with δ_{nth} near-zero (see Ball et al. 2016). Furthermore, particle-in-cell simulations show that electrons accelerated in reconnection events attain progressively harder energy spectra as the magnetization of the plasma increases (Sironi & Spitkovsky 2014). This will again have a strong impact on variability. We plan to investigate this issue in a future study.

Finally, we note that many of the results presented here are specific to accretion at ultra-low mass accretion rates. At higher accretion rates, the radiative efficiency will be larger, as will the scattering optical depth, which will increase the importance of inverse Compton scattering. Klein-Nishina corrections, which are included in the code but had a minimal effect in the present study, may become more important for the nonthermal electrons. Also, while feedback from nonthermal electrons on the other gas quantities was found to be negligible in this work, it is likely to have more of an effect at higher accretion rates, or with different injection prescriptions. Two-temperature simulations with thermal electrons and ions show that, at higher accretion rates, radiation from thermal electrons cools the gas more effectively and causes the disc to be thinner (Sądowski et al. 2017; Sądowski & Gaspari 2017). This effect is likely to be enhanced when nonthermal electrons are included.

ACKNOWLEDGEMENTS

We thank Jason Dexter for his help in using and modifying `grtrans` and the referee, Sean Ressler, for his helpful comments. AC was supported in part by NSF grant AST-1440254. RN was supported in part by NSF grant AST-1312651. AS acknowledges support for this work by NASA through Einstein Postdoctoral Fellowship number PF4-150126 awarded by the Chandra X-ray Center, which is operated by the Smithsonian Astrophysical Observatory for NASA under contract NAS8-03060. The authors acknowledge computational support from NSF via XSEDE resources (grant TG-AST080026N) and from the PL-Grid Infrastructure.

REFERENCES

Agol E., 2000, *ApJL*, 538, L121

- Baganoff F. K., et al., 2003, *ApJ*, 591, 891
- Ball D., Özel F., Psaltis D., Chan C.-k., 2016, *ApJ*, 826, 77
- Barrière N. M., et al., 2014, *ApJ*, 786, 46
- Blandford R. D., Begelman M. C., 1999, *MNRAS*, 303, L1
- Bower G. C., Wright M. C. H., Falcke H., Backer D. C., 2003, *ApJ*, 588, 331
- Broderick A. E., Loeb A., 2006, *MNRAS*, 367, 905
- Buchler J. R., Yueh W. R., 1976, *ApJ*, 210, 440
- Chan C.-k., Psaltis D., Özel F., Medeiros L., Marrone D., Sađowski A., Narayan R., 2015, *ApJ*, 812, 103
- Chandra M., Foucart F., Gammie C. F., 2017, *ApJ*, 837, 92
- Chandra M., Gammie C. F., Foucart F., Quataert E., 2015, *ApJ*, 810, 162
- Chandrasekhar S., 1939, *An introduction to the study of stellar structure*
- Chatzopoulos S., Fritz T. K., Gerhard O., Gillessen S., Wegg C., Genzel R., Pfuhl O., 2015, *MNRAS*, 447, 948
- Dexter J., 2016, *MNRAS*, 462, 115
- Dexter J., Agol E., Fragile P. C., McKinney J. C., 2010, *ApJ*, 717, 1092
- Dodds-Eden K., et al., 2009, *ApJ*, 698, 676
- Dodds-Eden K., et al., 2011, *ApJ*, 728, 37
- Doeleman S. S., et al., 2008, *Nature*, 455, 78
- Dolence J. C., Gammie C. F., Mościbrodzka M., Leung P. K., 2009, *ApJS*, 184, 387
- Eckart A., et al., 2006, *A&A*, 450, 535
- Falcke H., Goss W. M., Matsuo H., Teuben P., Zhao J.-H., Zylka R., 1998, *ApJ*, 499, 731
- Foucart F., Chandra M., Gammie C. F., Quataert E., 2016, *MNRAS*, 456, 1332
- Fouka M., Ouichaoui S., 2013, *Research in Astronomy and Astrophysics*, 13, 680
- Gammie C. F., McKinney J. C., Tóth G., 2003, *ApJ*, 589, 444
- Genzel R., Schödel R., Ott T., Eckart A., Alexander T., Lacombe F., Rouan D., Aschenbach B., 2003, *Nature*, 425, 934
- Gillessen S., Eisenhauer F., Trippe S., Alexander T., Genzel R., Martins F., Ott T., 2009, *ApJ*, 692, 1075
- Ginzburg V. L., Syrovatskii S. I., 1964, *The Origin of Cosmic Rays*
- Guo X., Sironi L., Narayan R., 2014, *ApJ*, 794, 153
- Hawley J. F., 2000, *ApJ*, 528, 462
- Howes G. G., 2010, *MNRAS*, 409, L104
- Ichimaru S., 1977, *ApJ*, 214, 840
- Leung P. K., Gammie C. F., Noble S. C., 2011, *ApJ*, 737, 21
- Levermore C. D., 1984, *JQSRT*, 31, 149
- Lindquist R. W., 1966, *Annals of Physics*, 37, 487
- Mahadevan R., Quataert E., 1997, *ApJ*, 490, 605
- Manolakou K., Horns D., Kirk J. G., 2007, *A&A*, 474, 689
- Mao S. A., Dexter J., Quataert E., 2016, *MNRAS*
- Marrone D. P., Moran J. M., Zhao J.-H., Rao R., 2007, *ApJL*, 654, L57
- McKinney J. C., Tchekhovskoy A., Blandford R. D., 2012, *MNRAS*, 423, 3083
- McKinney J. C., Tchekhovskoy A., Sađowski A., Narayan R., 2014, *MNRAS*, 441, 3177
- Mihalas D., Mihalas B. W., 1984, *Foundations of radiation hydrodynamics*
- Moderski R., Sikora M., Coppi P. S., Aharonian F., 2005, *MNRAS*, 363, 954
- Mościbrodzka M., Falcke H., Shiokawa H., Gammie C. F., 2014, *A&A*, 570, A7
- Mościbrodzka M., Gammie C. F., Dolence J. C., Shiokawa H., Leung P. K., 2009, *ApJ*, 706, 497
- Narayan R., Mahadevan R., Grindlay J. E., Popham R. G., Gammie C., 1998, *ApJ*, 492, 554
- Narayan R., Sađowski A., Penna R. F., Kulkarni A. K., 2012, *MNRAS*, 426, 3241
- Narayan R., Yi I., 1995a, *ApJ*, 444, 231
- Narayan R., Yi I., 1995b, *ApJ*, 452, 710
- Narayan R., Zhu Y., Psaltis D., Sađowski A., 2016, *MNRAS*, 457, 608
- Neilsen J., et al., 2013, *ApJ*, 774, 42
- Özel F., Psaltis D., Narayan R., 2000, *ApJ*, 541, 234
- Pandya A., Zhang Z., Chandra M., Gammie C. F., 2016, *ApJ*, 822, 34
- Porquet D., et al., 2008, *A&A*, 488, 549
- Quataert E., Narayan R., 1999, *ApJ*, 520, 298
- Quataert E., Narayan R., Reid M. J., 1999, *ApJL*, 517, L101
- Rees M. J., Begelman M. C., Blandford R. D., Phinney E. S., 1982, *Nature*, 295, 17
- Ressler S. M., Tchekhovskoy A., Quataert E., Chandra M., Gammie C. F., 2015, *MNRAS*, 454, 1848
- Ressler S. M., Tchekhovskoy A., Quataert E., Gammie C. F., 2017, *MNRAS*, 467, 3604
- Rybicki G. B., Lightman A. P., 1986, *Radiative Processes in Astrophysics*
- Sađowski A., Gaspari M., 2017, *MNRAS*, 468, 1398
- Sađowski A., Narayan R., 2015, *MNRAS*, 454, 2372
- Sađowski A., Narayan R., 2016, *MNRAS*, 456, 3929
- Sađowski A., Narayan R., McKinney J. C., Tchekhovskoy A., 2014, *MNRAS*, 439, 503
- Sađowski A., Narayan R., Penna R., Zhu Y., 2013, *MNRAS*, 436, 3856
- Sađowski A., Narayan R., Tchekhovskoy A., Abarca D., Zhu Y., McKinney J. C., 2015, *MNRAS*, 447, 49
- Sađowski A., Narayan R., Tchekhovskoy A., Zhu Y., 2013, *MNRAS*, 429, 3533
- Sađowski A., Wielgus M., Narayan R., Abarca D., McKinney J. C., Chael A., 2017, *MNRAS*, 466, 705
- Shcherbakov R. V., Penna R. F., McKinney J. C., 2012, *ApJ*, 755, 133
- Sironi L., Spitkovsky A., 2011, *ApJ*, 726, 75
- Sironi L., Spitkovsky A., 2014, *ApJL*, 783, L21
- Stepney S., Guilbert P. W., 1983, *MNRAS*, 204, 1269
- Tchekhovskoy A., Narayan R., McKinney J. C., 2010, *ApJ*, 711, 50
- Webb G. M., 1985, *ApJ*, 296, 319
- Webb G. M., 1989, *ApJ*, 340, 1112
- Yuan F., Narayan R., 2014, *ARAA*, 52, 529
- Yuan F., Quataert E., Narayan R., 2003, *ApJ*, 598, 301
- Yuan F., Quataert E., Narayan R., 2004, *ApJ*, 606, 894
- Yusef-Zadeh et al., 2006, *ApJ*, 644, 198
- Zhu Y., Narayan R., Sađowski A., Psaltis D., 2015, *MNRAS*, 451, 1661